SUPPLEMENTARY INFORMATION

Wavenumber lock-in in buckled elastic structures: an analogue to parametric instabilities

— H.E. Read, — G. Risso, — A. Djellouli, — K. Bertoldi, — A. Lazarus

I. PARAMETRIC PENDULUM

We begin by considering the inverted pendulum shown in Fig. 1 of the main text, or Fig. S1 here.

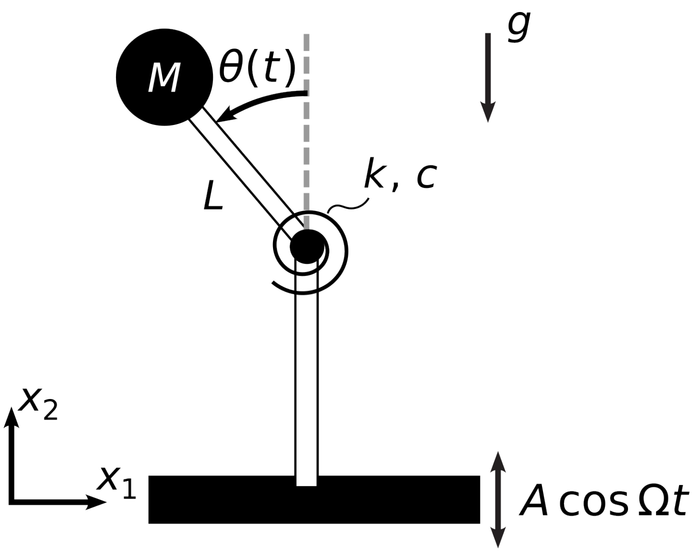

Fig. S1. Schematic of an inverted pendulum with a shaking base. We study the stability and spectral response of $\theta(t)$ as a function of amplitude and period of the shaking.

This pendulum has mass M and length L and is connected to a rigid base via a rotational spring with stiffness k and a rotational dashpot with damping coefficient c. Additionally, the base of this pendulum is oscillated by applying a harmonic displacement along the vertical direction with amplitude A and frequency Ω

$$u_{\text{applied}} = A\cos\Omega t. \tag{S1}$$

The equation of motion for such a system is given by [1].

$$\ddot{\theta} + \frac{c}{ML^2}\dot{\theta} + \frac{k}{ML^2}\theta + \left(\frac{A\Omega^2}{L}\cos\Omega t - \frac{g}{L}\right)\sin\theta = 0, \tag{S2}$$

where g denotes the gravitational acceleration, θ is the angle from the vertical to the pendulum and $\dot{\theta} = \dfrac{\mathrm{d}\theta}{\mathrm{d}t}$. We see from Eq. (S2) that in the absence of forcing (i.e. $A = 0$) and for small oscillations this system's undamped natural frequency is

$$\omega_0 = \left(\frac{k}{ML^2} - \frac{g}{L}\right)^{1/2}. \tag{S3}$$

Next, we nondimensionalize Eq. (S2) to reduce the number of independent variables from six (c, k, M, L, A, Ω) to three. Toward this end, we begin by introducing the normalized time

$$\tau = \omega_0 t. \tag{S4}$$

Substitution of Eq. (S4) into Eq. (S2) yields

$$\omega_0^2\theta'' + \frac{c}{ML^2}\omega_0\theta' + \frac{k}{ML^2}\theta + \left(\frac{A\Omega^2}{L}\cos\frac{\Omega}{\omega_0}\tau - \frac{g}{L}\right)\sin\theta = 0, \tag{S5}$$

where $\theta' = \dfrac{\mathrm{d}\theta}{\mathrm{d}\tau}$ denotes a derivative with respect to τ rather than t. Next, we multiply both sides of Eq. (S5) by $1/\omega_0^2$ and linearize it about $\theta_0 = 0$ by assuming $\sin\theta \approx \theta$, yielding

$$\frac{1}{\omega_0^2}\left[\omega_0^2\theta'' + \frac{c}{ML^2}\omega_0\theta' + \frac{k}{ML^2}\theta + \left(\frac{A\Omega^2}{L}\cos\frac{\Omega}{\omega_0}\tau - \frac{g}{L}\right)\theta\right] = \frac{1}{\omega_0^2}\cdot 0 \tag{S6}$$

$$\theta'' + \frac{c}{ML^2}\frac{1}{\omega_0}\theta' + \frac{1}{\omega_0^2}\underbrace{\left(\frac{k}{ML^2} - \frac{g}{L}\right)}_{\omega_0^2}\theta + \frac{1}{\omega_0^2}\frac{A\Omega^2}{L}\cos\frac{\Omega}{\omega_0}\tau\,\theta = 0 \tag{S7}$$

$$\theta'' + \frac{c}{\omega_0 ML^2}\theta' + \left(1 + \frac{A\Omega^2}{L\omega_0^2}\cos\frac{\Omega}{\omega_0}\tau\right)\theta = 0. \tag{S8}$$

Eq. (S8) shows that the system's behavior is governed by three dimensionless quantities: the normalized driving frequency,

$$\bar{\Omega} = \frac{\Omega}{\omega_0}, \tag{S9}$$

the normalized amplitude,

$$\bar{A} = \frac{A\Omega^2}{L\omega_0^2}, \tag{S10}$$

and the normalized damping factor,

$$\bar{C} = \frac{c}{\omega_0 ML^2}. \tag{S11}$$

Substitution of Eqs. (S9), (S10) and (S11) into Eq. (S8) yields

$$\theta'' + \bar{C}\theta' + \left(1 + \bar{A}\cos\bar{\Omega}\tau\right)\theta = 0, \tag{S12}$$

which is the linearized and non-dimensionalized equation of motion for the system about $\theta_0 = 0$.

Finally, we rewrite Eq. (S12) as a first order system of equations, which is the form used for Floquet analysis (discussed further in Section III)

$$\begin{pmatrix}\theta' \\ \theta''\end{pmatrix} = \begin{pmatrix}0 & 1 \\ -1 - \bar{A}\cos\bar{\Omega}\tau & -\bar{C}\end{pmatrix}\begin{pmatrix}\theta \\ \theta'\end{pmatrix}. \tag{S13}$$

II. MODULATED WINKLER FOUNDATION

Here we consider an elastic beam with bending modulus EI on a linear Winkler foundation with a periodic stiffness per unit length (see Fig. 1 of main text or Fig. S2 here.)

$$K(x_1) = K_0 + K_1 \cos \Omega x_1, \tag{S14}$$

where K_0 is the base stiffness, K_1 is the amplitude of modulation, and Ω is the frequency of modulation, with an associated wavelength $\lambda = 2\pi/\Omega$.

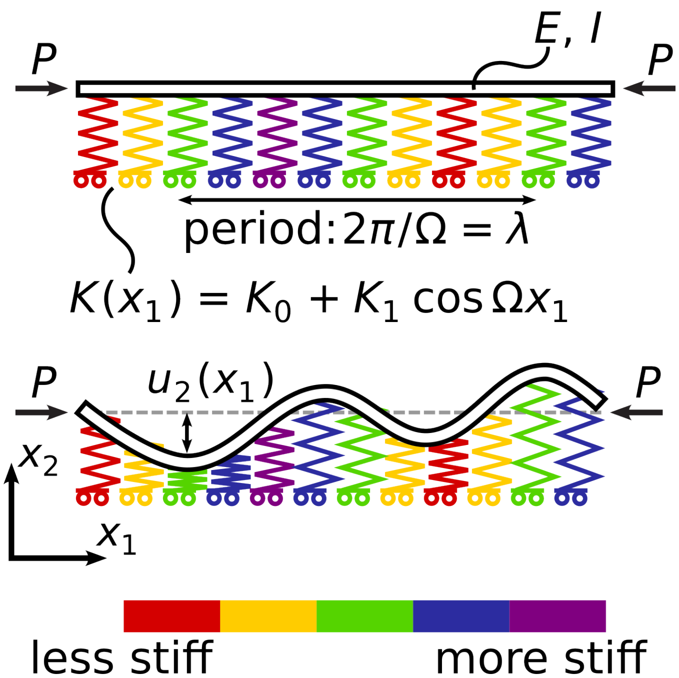

Fig. S2. Schematic of the modulated Winkler foundation. We study the buckling patters $y(x)$ as a function of period and modulation of foundation stiffness.

We investigate the buckling patterns of the beam—the y-deflection—under an axial load P. When modeling the beam as an inextensible EulerBernoulli beam, the linearized equilibrium equation governing its transverse deflection about $u_2(x_1) = 0$ is given by [2, 3]

$$EI \frac{\mathrm{d}^4 u_2}{\mathrm{d}{x_1}^4} + P \frac{\mathrm{d}^2 u_2}{\mathrm{d}{x_1}^2} + (K_0 + K_1 \cos \Omega x_1)\, u_2(x_1) = 0. \tag{S15}$$

Like the non-dimensionalized equation of motion for the inverted pendulum (Eq. (S12)), this is an ordinary differential equation with a periodic coefficient in the zeroth-order term. We know that for an elastic beam on a Winkler foundation with constant stiffness per unit length $K(x_1) = K_0$, buckling instability is triggered at a critical axial force [2]

$$P_{cr} = 2\sqrt{K_0 EI}, \tag{S16}$$

leading to the formation of a sinusoidal pattern with wavelength

$$\lambda_0 = 2\pi \left(\frac{EI}{K_0}\right)^{1/4}. \tag{S17}$$

As in Section I, we non-dimensionalize Eq. (S15) to reduce the number of independent variables from six (E, I, P, K_0, K_1, Ω) to three. We begin by introducing the normalized coordinate

$$\bar{x}_1 = \frac{x_1}{\lambda_0}, \tag{S18}$$

Substitution of Eq. (S18) into Eq. (S15) yields

$$\frac{EI}{\lambda_0^4} u_2^{(4)} + \frac{P}{\lambda_0^2} u_2'' + \left(K_0 + K_1 \cos \Omega\lambda_0 \bar{x}\right)\, u_2 = 0 \tag{S19}$$

$$EI \cdot \frac{K_0}{(2\pi)^4 EI} u_2^{(4)} + P \cdot \frac{\sqrt{K_0}}{(2\pi)^2\sqrt{EI}} u_2'' + \left(K_0 + K_1 \cos \Omega\lambda_0 \bar{x}\right)\, u_2 = 0, \tag{S20}$$

where derivatives u_2'' and $u_2^{(4)}$ are taken with respect to $\bar{x}_1$. We now multiply both sides by $(2\pi)^4/K_0$. This gives

$$\frac{(2\pi)^4}{K_0}\left[\frac{K_0}{(2\pi)^4} u_2^{(4)} + P \cdot \frac{\sqrt{K_0}}{(2\pi)^2\sqrt{EI}} u_2'' + \left(K_0 + K_1 \cos \Omega\lambda_0 \bar{x}_1\right)\, u_2\right] = \frac{(2\pi)^4}{K_0} \cdot 0 \tag{S21}$$

$$u_2^{(4)} + \frac{P(2\pi)^2}{\sqrt{K_0 EI}} u_2'' + \left(16\pi^4 + \frac{16\pi^4 K_1}{K_0} \cos \Omega\lambda_0 \bar{x}_1\right) u_2 = 0. \tag{S22}$$

Eq. (S22) shows that the Winkler foundations behavior is governed by three dimensionless quantities: the normalized axial load

$$\bar{P} = \frac{4\pi^2 P}{\sqrt{K_0 EI}} = 8\pi^2 \frac{P}{P_{cr}}, \tag{S23}$$

the nondimensionalized amplitude of modulation stiffness

$$\bar{K} = \frac{K_1}{K_0}, \tag{S24}$$

and the nondimensionalized frequency of modulation

$$\bar{\Omega} = \Omega\lambda_0. \tag{S25}$$

We then substitute Eqs. (S23), (S24), and (S25) into Eq. (S22), which yields

$$u_2^{(4)} + \bar{P} u_2'' + 16\pi^4 \left(1 + \bar{K} \cos \bar{\Omega}\bar{x}\right)\, u_2 = 0, \tag{S26}$$

which is the non-dimensionalized equation of motion for the system about $u_2(x_1) = 0$.

Finally, we rewrite Eqn. (S26) as a first order system of equations, which is the form used for Floquet analysis (discussed further in Section III)

$$\begin{pmatrix} u_2' \\ u_2'' \\ u_2''' \\ u_2^{(4)} \end{pmatrix} = \begin{pmatrix} 0 & 1 & 0 & 0 \\ 0 & 0 & 1 & 0 \\ 0 & 0 & 0 & 1 \\ -16\pi^4 - 16\pi^4 \bar{K} \cos \bar{\Omega}\bar{x}_1 & 0 & -\bar{P} & 0 \end{pmatrix} \begin{pmatrix} u_2 \\ u_2' \\ u_2'' \\ u_2''' \end{pmatrix}. \tag{S27}$$

III. FLOQUET THEORY

Equations (S12) and (S26) show that the perturbed motion of both the parametric pendulum and the modulated Winkler foundation are governed by linear differential equations with periodically varying coefficients. To analyze such equations, we use Floquet theory [4]. Floquet theory provides a framework for analyzing Hill equations—that is, linear differential equations of order N with periodically varying coefficients of the form

$$y^{(N)} + a_{N-1}(\xi)y^{(N-1)} + \cdots + a_1(\xi)y' + a_0(\xi)y = 0, \tag{S28}$$

where the coefficients $a_i(\xi)$ are all periodic functions with a common period T. As a first step to determine our solution, we rewrite Eq. (S28) as a first order system of equations,

$$Y' = J(\xi)\, Y, \tag{S29}$$

where $Y \in \mathbb{R}^N$. Since all our coefficients a_i are T-periodic, it follows that $J(\xi)$ is also T-periodic. Specific forms of the matrix J for the parametric pendulum and the modulated Wrinkler foundation are given in Eqs. (S13) and (S27), respectively. Floquet theory tells us that solutions to Eq. (S29) take the form

$$Y(\xi) = \sum_{n=1}^{N} r_n(\xi) \cdot e^{s_n \xi}, \tag{S30}$$

where $r_n(\xi) \in \mathbb{C}^N$ is periodic with period T and $s_n \in \mathbb{C}$ are the Floquet exponents [1, 5]. Each $r_n(\xi) \cdot e^{s_n \xi}$ term is called a Floquet form; since $r_n(\xi)$ is periodic, the stability of each Floquet form depends entirely on the $e^{s_n \xi}$ term, or more particularly, the real component of s_n. Depending on the initial or boundary conditions of Eq. (S29), s_n with real parts greater than 0 could lead to growing or unbounded $Y(\xi)$ as $\xi \to \infty$. In this work, we generally only calculate the Floquet exponents to understand the behavior of our system rather than calculate the whole solution. As a note, Floquet exponents are not unique; since $e^{ia} = e^{i(a+2\pi)}$ for $a \in \mathbb{R}$, the imaginary parts of our s_n are not unique. This means that if $s = a + bi$ is a valid Floquet exponent, so is $s = a + (b + 2\pi k/T)i$ for $k \in \mathbb{Z}$.

There are a few methods to calculate the Floquet exponents, for example, the Monodromy matrix method [1, 5] or Hill (spectral) method [6–8]. Here, we use the Hill method. In this method, we transform both our matrix $J(\xi)$ and states Y and Y' into the frequency space. More specifically, $J(\xi)$ and $Y(\xi)$ transform into

$$J(\xi) = J_0 e^{0i\Omega\xi} + J_1 e^{i\Omega\xi} + J_{-1} e^{-i\Omega\xi} + J_2 e^{2i\Omega\xi} + J_{-2} e^{-2i\Omega\xi} + \ldots, \tag{S31}$$

and

$$\hat{Y}(\xi) = \sum_{h\in\mathbb{Z}} \sum_{n=1}^{N} r_n^h \cdot e^{(ih\Omega + s_n)\xi}, \tag{S32}$$

where $\Omega = 2\pi/T$ is the fundamental frequency of $J(\xi)$ and the r_n^h are N-dimensional complex vectors that are the h^{th} harmonics of the periodic function $r_n(\bar{x}) = r_n(\bar{x} + \bar{\lambda})$ of the n^{th} Floquet form.

To reduce bulk in our equations, instead of inserting the full solution into Eq. (S29), we will instead use the ansatz

$$\hat{Y}(\xi) = \sum_{h\in\mathbb{Z}} r^h \cdot e^{(ih\Omega + s)\xi}. \tag{S33}$$

Substitution of Eqs. (S31) and (S33) into Eq. (S29) yields

$$0 = \sum_{h\in\mathbb{Z}} \left(J_0 + J_1 e^{i\Omega\xi} + J_{-1} e^{-i\Omega\xi} + J_2 e^{2i\Omega\xi} + J_{-2} e^{-2i\Omega\xi} + \ldots\right) r^h\, e^{(ih\Omega+s)\xi} - (ih\Omega + s)\, r^h\, e^{(ih\Omega+s)\xi}, \tag{S34}$$

which can be simplified to (by factoring out the $e^{s\xi}$ term)

$$0 = \sum_{h\in\mathbb{Z}} \left(J_0 + J_1 e^{i\Omega\xi} + J_{-1} e^{-i\Omega\xi} + J_2 e^{2i\Omega\xi} + J_{-2} e^{-2i\Omega\xi} + \dots\right) r^h\, e^{ih\Omega\xi} - (ih\Omega + s)\, r^h\, e^{ih\Omega\xi}. \tag{S35}$$

Now, we apply the harmonic balance method: if this whole equation is balanced, each $e^{ih\Omega\xi}$ term must also be balanced. We show a few terms around $h = 0$ to get an idea of the general pattern.

$$e^{0i\Omega\xi} : 0 = J_0 r^0 - (i\cancel{0\Omega} + s) r^0 + J_1 r^{-1} + J_{-1} r^1 + r^2 J_{-2} + J_2 r^{-2} + \dots \tag{S36}$$

$$e^{1i\Omega\xi} : 0 = J_0 r^1 - (i\Omega + s) r^1 + J_1 r^0 + J_{-1} r^2 + J_2 r^{-1} + J_{-2} r^3 + \dots \tag{S37}$$

$$e^{-1i\Omega\xi} : 0 = J_0 r^{-1} - (-i\Omega + s) r^{-1} + J_1 r^2 + J_{-1} r^0 + J_2 r^{-3} + J_{-2} r^1 + \dots \tag{S38}$$

$$e^{2i\Omega\xi} : 0 = J_0 r^2 - (2i\Omega + s) r^2 + J_1 r^1 + J_{-1} r^3 + J_2 r^0 + J_{-2} r^4 + \dots \tag{S39}$$

$$e^{-2i\Omega\xi} : 0 = J_0 r^{-2} - (-2i\Omega + s) r^{-2} + J_1 r^{-3} + J_{-1} r^{-1} + J_2 r^{-4} + J_{-2} r^0 + \dots \tag{S40}$$

We now use these gathered terms to rewrite Eq. (S35) in matrix form; we get

$$\left(\begin{bmatrix} \ddots & \vdots & \vdots & \vdots & \vdots & \vdots & \\ \cdots & J_0 + 2i\Omega\, I_n & J_{-1} & J_{-2} & J_{-3} & J_{-4} & \cdots \\ \cdots & J_1 & J_0 + i\Omega\, I_n & J_{-1} & J_{-2} & J_{-3} & \cdots \\ \cdots & J_2 & J_1 & J_0 & J_{-1} & J_{-2} & \cdots \\ \cdots & J_3 & J_2 & J_1 & J_0 - i\Omega\, I_n & J_{-1} & \cdots \\ \cdots & J_4 & J_3 & J_2 & J_1 & J_0 - 2\Omega\, I_n & \cdots \\ & \vdots & \vdots & \vdots & \vdots & \vdots & \ddots \end{bmatrix} - s\,\mathbf{I} \right) \begin{bmatrix} \vdots \\ r^{-2} \\ r^{-1} \\ r^0 \\ r^1 \\ r^2 \\ \vdots \end{bmatrix} = 0, \tag{S41}$$

or

$$(\mathbf{H} - s\,\mathbf{I})\,\mathbf{r} = \mathbf{0}, \tag{S42}$$

where $\mathbf{I}$ is the identity matrix.

We see from Eq. (S42) that Eq. (S35) can be rewritten as an eigenvalue-eigenvector problem of $\mathbf{H}$. When we retain an infinite number of terms, Eq. (S42) is identical to Eq. (S35). Practically however, we truncate the Hill matrix to M harmonics—between r^{-M} to r^M with M between 5–9. This leads to a system of size $(2M+1)N$, where N is the order of the considered differential equation. Since this truncation can introduce incorrect eigenvalues [8], we keep only eigenvalues s within the first Brillouin zone

$$|\operatorname{Im} s| < \frac{\Omega}{2} + 10^{-M}, \tag{S43}$$

up to a tolerance of 10^{-M}. As long as we pick M large enough this truncation and sorting is guaranteed to give us accurate eigenvalues [9].

Below, we discuss problem-specific considerations for the inverted pendulum and the periodic Winkler foundation.

A. Floquet theory for the Inverted Pendulum

Here, we apply Floquet theory to the inverted pendulum considered in Section I. It follows from Eq. (S13) that the J matrix for this system is given by

$$J(\tau) = \begin{pmatrix} 0 & 1 \\ -1 - \bar{A}\cos\bar{\Omega}\tau & -\bar{C} \end{pmatrix}. \tag{S44}$$

Following the procedure described in the above section, we rewrite $J(\tau)$ as a Fourier expansion to obtain

$$\begin{pmatrix} 0 & 1 \\ -1-\bar{A}\cos\bar{\Omega}\tau & -\bar{C} \end{pmatrix} = \underbrace{\begin{pmatrix} 0 & 1 \\ -1 & -\bar{C} \end{pmatrix}}_{J_0} 1 + \underbrace{\begin{pmatrix} 0 & 0 \\ -\bar{A}/2 & 0 \end{pmatrix}}_{J_1} e^{i\bar{\Omega}\tau} + \underbrace{\begin{pmatrix} 0 & 0 \\ -\bar{A}/2 & 0 \end{pmatrix}}_{J_{-1}} e^{-i\bar{\Omega}\tau}. \tag{S45}$$

Note that $J_1 = J_{-1}$ due to the cosine in $J(\tau)$. Using the J_i defined in Eq. (S45), we can construct our $\mathbf{H}$ matrix using $M = 9$ as described in Eq. (S41) and then calculate its eigenvalues. While this gives $(2M+1)N = 38$ eigenvalues, we keep only those which satisfy Eq. (S43).

In Fig. S3 we present results for an inverted pendulum with dimensionless damping factor $\bar{C} = 0.001$. Specifically, in Fig. S3a-b, we report the evolution as a function of $\bar{T}/(2\pi)$ of the maximum real and imaginary components of all calculated Floquet exponents in the first Brillouin zone, $\max(\mathrm{Re}(s))$ and $\max(\mathrm{Im}(s))$, for a few values of normalized amplitude $\bar{A}$. Further, in Fig. S3c-d, we report the evolution of $\max(\mathrm{Re}(s))$ and $\max(\mathrm{Im}(s))$ as a function of $\bar{T}/(2\pi)$ and $\bar{A}$.

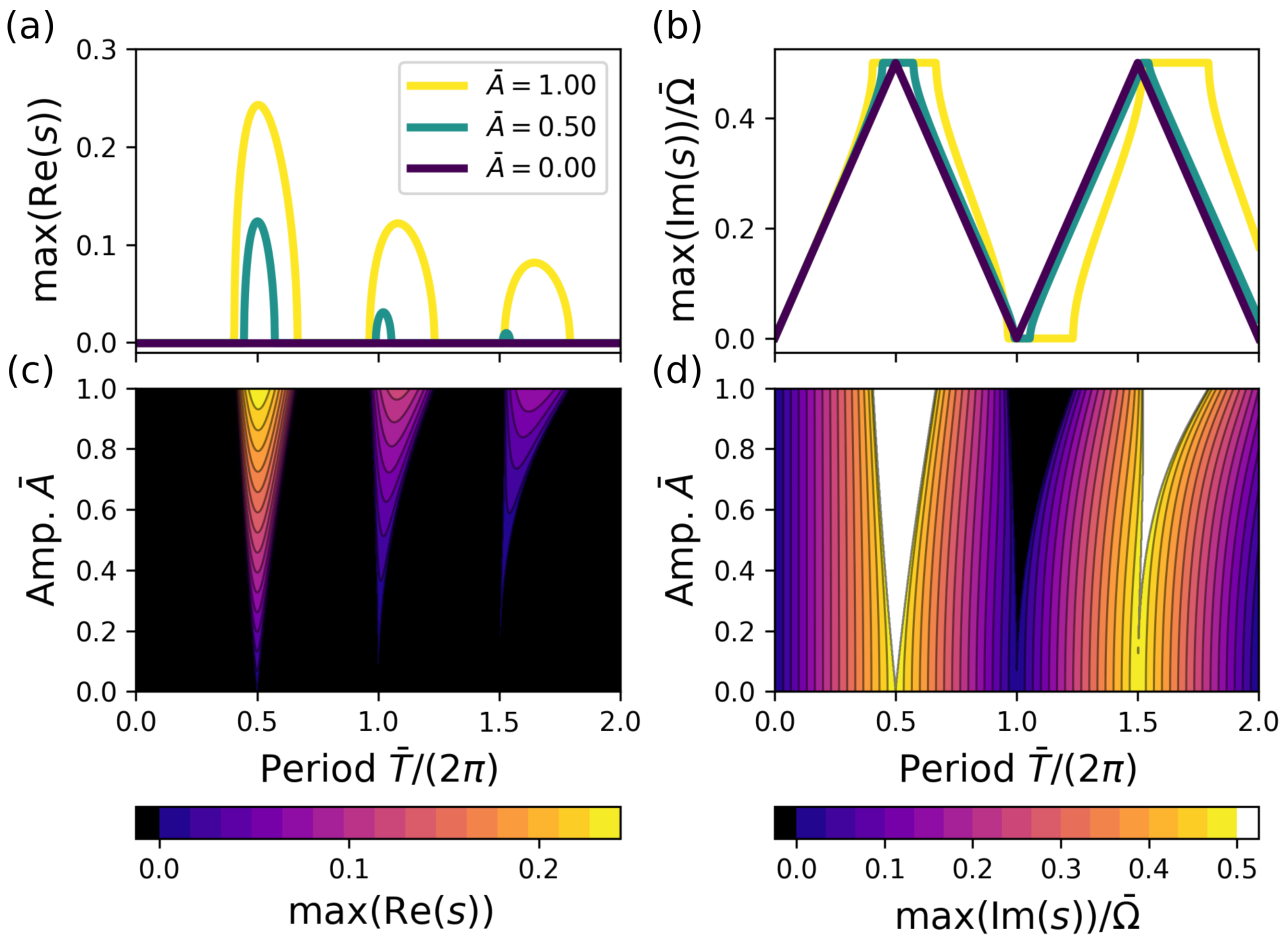

Fig. S3. **Floquet exponents for the inverted pendulum** Maximum real (a) and imaginary (b) components of Floquet exponents within the first Brillouin zone for our inverted pendulum problem for a few values of non-dimensionalized amplitude, $\bar{A}$, as a function of non-dimensionalized period, $\bar{T}/(2\pi)$. (c) and (d) are max(Re(s) and max(Im(s)) in the modulation parameter space $\bar{A}$ and $\bar{T}/(2\pi)$; we can clearly see the emergence of stability tongues which are known to exist for this problem.

Two key features emerge from these plots. First, for certain ranges of $\bar{T}$, the maximum real part of the Floquet exponents, $\max(\mathrm{Re}(s))$, is positive. Since this is an initial value problem, the presence of any Floquet exponent with a positive real part indicates an exponentially growing mode in time, implying that the trivial solution $\theta(\tau)=0$ solution is unstable. When we plot $\max(\mathrm{Re}(s))$ in the full $\bar{A}$–$\bar{T}$ parameter space, we see the emergence of instability tongues (Fig. S3c); these are called parametric instability regions in a dynamic system like the pendulum. Second, in the regimes where the solution is unstable, we have either $\max(\mathrm{Im}(s))=0$ or $\max(\mathrm{Im}(s))/\bar{\Omega}=0.5$. While the real parts of the Floquet exponents determine the stability of the system, the imaginary parts provide insight into the spectral characteristics of the response. We recall the Fourier transform of our solution (Eq. (S33)) modified to account for viscous damping [1]

$$\hat{\theta}(\tau)=\sum_{h\in\mathbb{Z}} r^h\cdot e^{(ih\bar{\Omega}+s-\bar{C}/2)\tau}+\sum_{h\in\mathbb{Z}} r^{*h}\cdot e^{(ih\bar{\Omega}-s-\bar{C}/2)\tau}, \tag{S46}$$

where r^{*h} denotes the complex conjugate of r^h. From Eq. (S46), we can see that when $+\,\mathrm{Im}(s)$ and $-\,\mathrm{Im}(s)$ are separated by an integer multiple of $\bar{\Omega}$, the frequency spectrum contains frequencies that are integer multiples of a fundamental frequency, so our solution is periodic. More specifically, when $\mathrm{Im}(s)/\bar{\Omega}=0$, θ is periodic with period $\bar{T}$, while when $\mathrm{Im}(s)/\bar{\Omega}=0.5$, θ is periodic with period $2\bar{T}$. This phenomenon is called "frequency lock-in", as the output frequency of the solution locks into a half or a full fundamental frequency of the driving frequency. Due to the structure of our problem, when we have frequency lock-in, $\max(\mathrm{Re}(s)-\bar{C})$ is positive and the solution grows unbounded with time. By contrast, when the imaginary components $\pm\,\mathrm{Im}(s)$ of our Floquet exponents are not separated by an integer multiple of $\bar{\Omega}$, i.e., $\mathrm{Im}(s)/\bar{\Omega}\in(0,0.5)$, the frequency spectrum of the solution contains frequencies that are incommensurate (non-integer ratios); the spectrum includes combinations of base frequencies without a single common period, so our solution is quasi-periodic. In these regions, $\mathrm{Re}(s)=-\bar{C}/2$, so the solution is also underdamped.

B. Floquet theory for the Periodic Winkler Foundation

Here, we apply Floquet theory to the periodic Winkler foundation considered in Section. I. It follows from Eq. (S27) that the J matrix for this system is given by

$$\mathbf{J}(\bar{x}_1)=\begin{pmatrix} 0 & 1 & 0 & 0\\ 0 & 0 & 1 & 0\\ 0 & 0 & 0 & 1\\ -16\pi^4-16\pi^4\bar{K}\cos\bar{\Omega}\bar{x}_1 & 0 & -\bar{P} & 0\end{pmatrix}. \tag{S47}$$

Following the procedure described in the above section, we first rewrite $J(\bar{x})$ as a Fourier expansion to obtain

$$\begin{pmatrix} 0 & 1 & 0 & 0\\ 0 & 0 & 1 & 0\\ 0 & 0 & 0 & 1\\ -16\pi^4-16\pi^4\bar{K}\cos\bar{\Omega}\bar{x}_1 & 0 & -\bar{P} & 0\end{pmatrix}=\underbrace{\begin{pmatrix} 0 & 1 & 0 & 0\\ 0 & 0 & 1 & 0\\ 0 & 0 & 0 & 1\\ -16\pi^4 & 0 & -\bar{P} & 0\end{pmatrix}}_{J_0}1+\underbrace{\begin{pmatrix} 0 & 0 & 0 & 0\\ 0 & 0 & 0 & 0\\ 0 & 0 & 0 & 0\\ -8\pi^2\bar{K} & 0 & 0 & 0\end{pmatrix}}_{J_1}e^{i\bar{\Omega}\bar{x}_1}+\underbrace{\begin{pmatrix} 0 & 0 & 0 & 0\\ 0 & 0 & 0 & 0\\ 0 & 0 & 0 & 0\\ -8\pi^2\bar{K} & 0 & 0 & 0\end{pmatrix}}_{J_{-1}}e^{-i\bar{\Omega}\bar{x}_1}. \tag{S48}$$

As with the inverted pendulum, we note that $J_1=J_{-1}$ due to the cosine in the driving term. Our parameters of interest are $\bar{K}$ and $\bar{\lambda}=2\pi/\bar{\Omega}$ and we choose to investigate $\bar{\lambda}\in[0.01,2]$ and $\bar{K}\in[0,0.5]$.

While in initial value problems, we must have all s with real component strictly less than 0 to have an asymptotically stable solution, our interpretation of Floquet exponents in the setting of boundary value problems is different. With

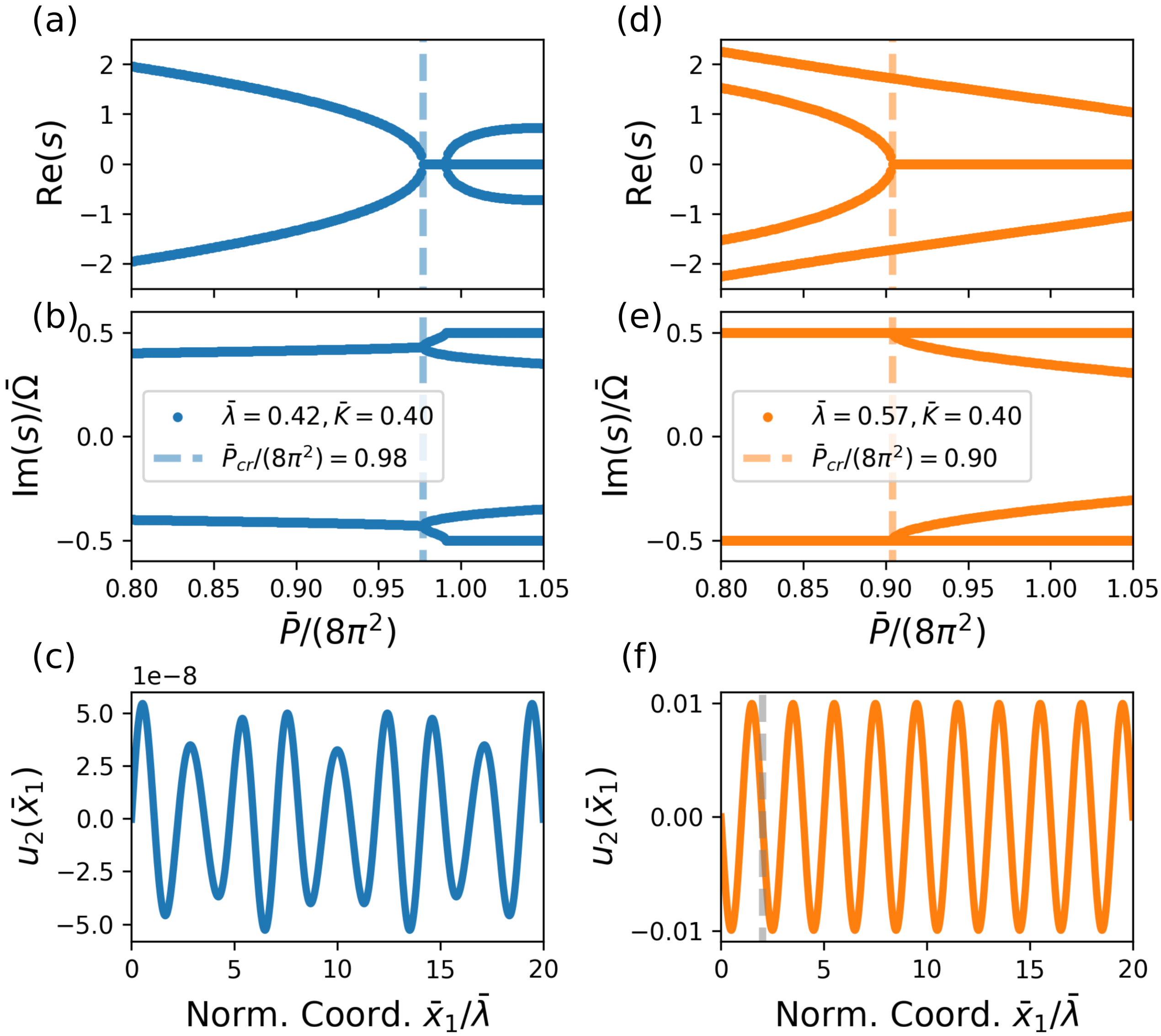

Fig. S4. **Floquet exponents as a function of loading.** Re(s) (a, d), Im(s) (b, e) as a function of axial loading $\bar{P}$ and output curves (c, f) for two values of period $\bar{\lambda}$, both at $\bar{K} = 0.4$. We see the critical $\bar{P}_{cr}$ occurs when a pair of s_i collapse to have real part equal to 0; this point is notated with a dashed line. The imaginary part of the Floquet exponents at the critical loading, $\bar{P}_{cr}$, tells us if our solutions is periodic (right side) or quasi-periodic (left side). The periodicity of the locked-in sample (f) is shown with a gray vertical line.

boundary conditions, any Floquet form $r(\xi) \cdot e^{s\xi}$ with $\mathrm{Re}(s) = 0$ will allow for a non trivial bounded solution, even if other Floquet forms have $\mathrm{Re}(s) > 0$, since the coefficients in front of those Floquet forms can become zero. Thus, in the Winkler foundation problem, we first calculate the minimal $\bar{P}$, called the critical buckling load, $\bar{P}_{cr}$, for which at least one Floquet exponent s has a real part equal to zero. In practice, to determine $\bar{P}_{cr}$, we compute the Floquet exponent s for increasing values of $\bar{P}$ and identify the load at which the real part of s falls below a threshold value, $\epsilon = 10^{-8}$. In Figs. S4a and S4d we report the evolution of $\mathrm{Re}(s)$ as a function of $\bar{P}$ for two foundations with $(\bar{K}, \bar{\lambda}) = (0.4, 0.42)$ and $(0.4, 0.57)$, respectively. For this two geometries we find that $\bar{P}_{cr} = 0.98 \cdot 8\pi^2$ and $0.90 \cdot 8\pi^2$, respectively.

Once the critical buckling load for a given geometry is determined, the imaginary parts of the Floquet exponents provide insight into the spectral content of the emerging buckling mode. In Figs. S5b and S5e, we plot the evolution of $\max(\mathrm{Im}(s))/\bar{\Omega}$ as a function of $\bar{P}$ for the same two geometries. For the first case ($\bar{\lambda} = 0.42$), at $\bar{P}_{cr}$ we find that $\max(\mathrm{Im}(s)) = 0.43$, indicating a quasi-periodic buckling mode (see Fig. S5c). In contrast, for the second case ($\bar{\lambda} = 0.57$), we have that $\max(\mathrm{Im}(s))/\bar{\Omega} = 0.5$ at $\bar{P}_{cr}$, corresponding to a frequency lock-in—similar to what is observed in the inverted pendulum—which results in a $2\bar{\lambda}$-periodic buckling mode (Fig. S5f). Finally, we note that, unlike the dynamic case, where periodic solutions grow unbounded in time and quasi-periodic ones decay (assuming positive damping), here both quasi-periodic and periodic solutions remain bounded and stable in the spatial variable $\bar{x}_1$.

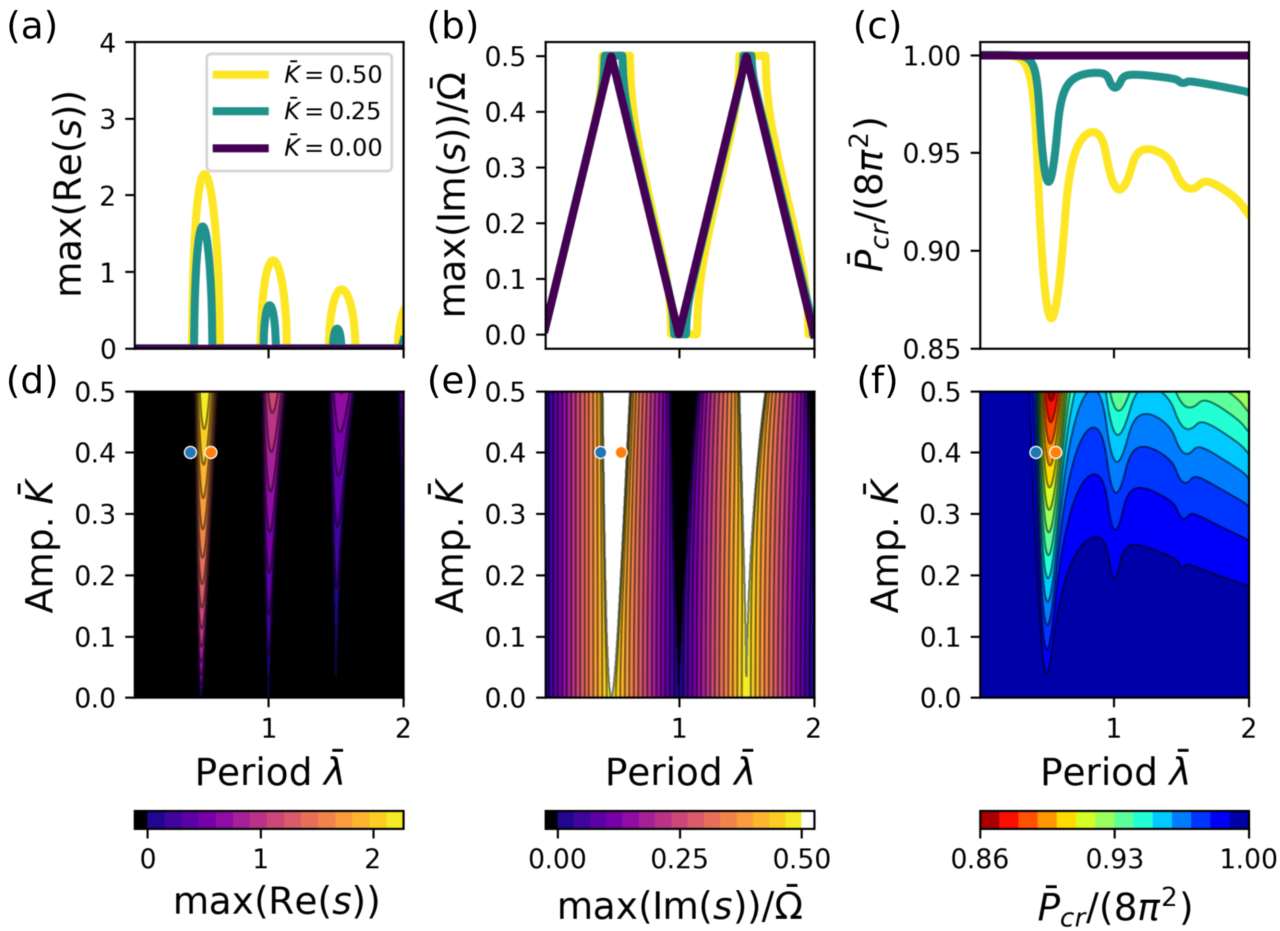

Fig. S5. **Real, imaginary components of s_n and the calculated critical applied load associated with each geometry.** In (a, b, c) we show the (a) maximum real component, (b) maximum imaginary component, and (c) calculated critical load as a function of $\bar{\lambda}$ for a few $\bar{K}$. In (d, e, f) we generalize these results in heat maps. Like for the inverted pendulum, we see the emergence of tongues where the maximum real component is positive. Again we see that in those tongues, the normalized imaginary component is either 0 or 0.5; we also see that in these tongues, there is a sharp decrease in necessary buckling force. In (d/e/f) we also plot the specific points seen in Fig. S4 in orange and blue.

Since the buckling load is also a function of our parameters, we plot $\bar{P}_{cr}$ normalized by the $8\pi^2$, the critical buckling force in the unmodulated case, i.e. when $\bar{K} = 0$. These example curves for different modulation amplitudes can be seen in Fig. S5c. Again, if we plot $\max(\mathrm{Re}(s))$ and $\max(\mathrm{Im}(s))$ as a function of amplitude, $\bar{K}$, and period of modulation, $\bar{\lambda}$, we see the emergence of lock-in tongues; these can be seen in Figs. S5d-f. We see that these lock-in tongues alternate between $\mathrm{Im}(s) = 0$, indicating $\bar{\lambda}$-periodic solutions, and $\mathrm{Im}(s) = 0.5$, indicating $2\bar{\lambda}$-periodic solutions. We also observe that the critical force, $\bar{P}_{cr}$, needed to buckle the structure decreases rapidly at the onset of of each lock-in tongue (Fig. S5f).

IV. FROM A MODULATED WINKLER FOUNDATION TO AN ELASTIC STRIP WITH MODULATED HEIGHT

The analysis of a beam resting on a modulated Winkler foundation indicates that wavenumber lock-in can occur in a purely static context, in close analogy with parametric instabilities in dynamical systems. This phenomenon arises in structures that (*i*) are governed by a homogeneous linear boundary-value problem with periodic coefficients sharing a common period, and (*ii*) admit non-trivial solutions that bifurcate from the trivial state once a critical value of the loading parameter is exceeded. While in Sections II and III we derive the solution for the modulated Winkler foundation, here we demonstrate that the modulation of height in an elastic strip leads to partial differential equations with periodic coefficients like Eq. (S26), as required to trigger wavenumber lock-in.

We begin by deriving the quasi-static equations of motion for a plate embedded in the three-dimensional space (x_1, x_2, x_3). The plate has thickness t in the x_3-direction, which is small compared to its characteristic dimensions in the x_1 and x_2 directions. To reduce the three-dimensional elasticity problem to an equivalent two-dimensional formulation defined on the mid-surface, we adopt the Kirchhoff–Love kinematic assumptions [10, 11]. Specifically, these assumptions are: (1) straight lines initially normal to the mid-surface of the plate remain straight after deformation; (2) these normals remain perpendicular to the deformed mid-surface, implying the absence of transverse shear deformation and hence vanishing transverse shear strains ($\gamma_{13} = \gamma_{23} = 0$); (3) the plate thickness remains unchanged during deformation, so that the normal strain in the thickness direction vanishes ($\varepsilon_{33} = 0$). Under the Kirchhoff–Love hypothesis, the displacement field is fully determined by the mid-surface displacement $\mathbf{u}(\mathbf{x})$ and may be written as

$$\begin{aligned} u_1(\mathbf{x}^{3D}) &= u_1(\mathbf{x}) - x_3 \frac{\partial u_3(\mathbf{x})}{\partial x_1}, \\ u_2(\mathbf{x}^{3D}) &= u_2(\mathbf{x}) - x_3 \frac{\partial u_3(\mathbf{x})}{\partial x_2}, \\ u_3(\mathbf{x}^{3D}) &= u_3(\mathbf{x}), \end{aligned} \tag{S49}$$

where $\mathbf{x}^{3D} = x_1\mathbf{e}_1 + x_2\mathbf{e}_2 + x_3\mathbf{e}_3$ denotes the position vector in three dimensions, $\mathbf{x} = x_1\mathbf{e}_1 + x_2\mathbf{e}_2$ is the corresponding mid-surface position vector, and $\mathbf{e}_i$ denote the Cartesian basis vectors.

Since our interest lies in the linear buckling modes of the elastic plate, we assume that the deformations are sufficiently small such that only the linearized strain components are retained. The strain tensor $\varepsilon_{ij}(\mathbf{x})$ is therefore defined as

$$\varepsilon_{ij}(\mathbf{x}) = \frac{1}{2}\left(\frac{\partial u_i(\mathbf{x}^{3D})}{\partial x_j} + \frac{\partial u_j(\mathbf{x}^{3D})}{\partial x_i} \right) \tag{S50}$$

with $i, j = 1, 2, 3$. Substitution of the Kirchhoff–Love displacement field given in Eq. (S49) into Eq. (S50) yields

$$\varepsilon_{11} = \frac{\partial u_1(\mathbf{x})}{\partial x_1} - x_3 \frac{\partial^2 u_3(\mathbf{x})}{\partial x_1^2}, \qquad \varepsilon_{22} = \frac{\partial u_2(\mathbf{x})}{\partial x_2} - x_3 \frac{\partial^2 u_3(\mathbf{x})}{\partial x_2^2}, \qquad \varepsilon_{12} = \frac{1}{2}\left(\frac{\partial u_1(\mathbf{x})}{\partial x_2} + \frac{\partial u_2(\mathbf{x})}{\partial x_1} - 2x_3 \frac{\partial^2 u_3(\mathbf{x})}{\partial x_1 \partial x_2} \right), \tag{S51}$$

and

$$\varepsilon_{13} = \varepsilon_{23} = \varepsilon_{33} = 0, \tag{S52}$$

which is consistent with the kinematic assumptions of thin plate theory. Next, we assume a plane stress state, which is appropriate for thin plates, so that

$$\sigma_{33} = \sigma_{13} = \sigma_{23} = 0, \tag{S53}$$

and a linear and isotropic constitutive relation between stress and strain, which is given by

$$\sigma_{\alpha\beta}(\mathbf{x}) = \frac{E}{1-\nu^2} \left[(1-\nu)\, \varepsilon_{\alpha\beta}(\mathbf{x}) + \nu\, \varepsilon_{\gamma\gamma}(\mathbf{x})\, \delta_{\alpha\beta} \right], \tag{S54}$$

where $\alpha, \beta = 1, 2$, E denotes Youngs modulus, ν is Poissons ratio, and δ_{ij} is the Kronecker delta.

The equilibrium equations governing the mid-surface of the plate can be decomposed into two independent sets of equations [10, 11]. First, in-plane equilibrium in the $x_1 - x_2$ plane requires

$$\frac{\partial N_{\alpha\beta}(\mathbf{x})}{\partial x_\beta} = 0, \tag{S55}$$

where the membrane force resultants are defined as

$$N_{\alpha\beta}(\mathbf{x}) = \int_{-t/2}^{t/2} \sigma_{\alpha\beta}(\mathbf{x})\, \mathrm{d}x_3 = t\sigma_{\alpha\beta}(\mathbf{x}). \tag{S56}$$

Second, in the absence of transverse loading, the equilibrium of transverse shear forces requires

$$\frac{\partial Q_\alpha(\mathbf{x})}{\partial x_\alpha} = 0. \tag{S57}$$

Note that the shear resultants Q_α are related to the bending moment resultants by

$$Q_\alpha(\mathbf{x}) = \frac{\partial M_{\alpha\beta}(\mathbf{x})}{\partial x_\beta}, \tag{S58}$$

where the bending moment resultants are given by

$$M_{\alpha\beta}(\mathbf{x}) = \int_{-t/2}^{t/2} \sigma_{\alpha\beta}(\mathbf{x})\, x_3\, \mathrm{d}x_3. \tag{S59}$$

Substituting Eqs. (S49)–(S54) into Eq. (S59) yields the classical KirchhoffLove constitutive relation

$$M_{\alpha\beta} = -D\left[(1-\nu)\frac{\partial^2 u_3}{\partial x_\alpha \partial x_\beta} + \nu \frac{\partial^2 u_3}{\partial x_\gamma \partial x_\gamma}\delta_{\alpha\beta}\right], \tag{S60}$$

where $\dfrac{\partial^2 u_3}{\partial x_\alpha \partial x_\beta}$ are the material curvatures and

$$D = \frac{Et^3}{12(1-\nu^2)} \tag{S61}$$

is the bending stiffness. Finally, substituting Eq. (S58) into Eq. (S57) leads to the out-of-plane equilibrium condition

$$\frac{\partial^2 M_{\alpha\beta}(\mathbf{x})}{\partial x_\alpha \partial x_\beta} = 0. \tag{S62}$$

In this work, we consider an initially flat plate subjected to in-plane loading and study its linear buckling behavior about the trivial base state characterized by zero out-of-plane displacement, $u_3(\mathbf{x}) = 0$ and vanishing bending moments, $M_{\alpha\beta}(\mathbf{x}) = 0$, in the absence of transverse external loads. As first step, we determine the membrane stress resultants $N^0_{\alpha\beta}(\mathbf{x})$ by solving the in-plane equilibrium equations given by Eq. (S55). Owing to the linearity of the in-plane equilibrium equations, the solution for an arbitrary load level κ can be written as

$$N^0_{\alpha\beta}(\mathbf{x}, \kappa) = \kappa\, N^0_{\alpha\beta}(\mathbf{x}), \tag{S63}$$

where $N^0_{\alpha\beta}(\mathbf{x})$ denotes the membrane force resultants corresponding to the reference load $\kappa = 1$. Then as second step, the critical buckling load and associated buckling mode are obtained by seeking nontrivial solutions of Eq. (S62), linearized about an infinitesimally deformed in-plane configuration [10, 11]. When we account for the deformation induced by the in-plane membrane stress resultants $N_{\alpha\beta}(\mathbf{x})$, the transverse shear resultant takes the form

$$Q_\alpha(\mathbf{x}) = \frac{\partial M_{\alpha\beta}(\mathbf{x})}{\partial x_\beta} + N_{\alpha\beta}(\mathbf{x})\frac{\partial u_3(\mathbf{x})}{\partial x_\beta}, \tag{S64}$$

where the second term accounts for the geometric contribution of the in-plane forces acting on the deformed mid-surface. Substituting Eq. (S64) into Eq. (S57) yields

$$\frac{\partial Q_\alpha(\mathbf{x})}{\partial x_\alpha} = \frac{\partial^2 M_{\alpha\beta}(\mathbf{x})}{\partial x_\alpha \partial x_\beta} + \frac{\partial}{\partial x_\alpha}\left(N_{\alpha\beta}(\mathbf{x})\frac{\partial u_3(\mathbf{x})}{\partial x_\beta}\right) = 0. \tag{S65}$$

The buckling equation is obtained by linearizing Eq.(S65) about the in-plane base state that is characterized by no out-of-plane displacement $u_3^0(\mathbf{x}) = 0$, no bending moments $M^0_{\alpha\beta}(\mathbf{x}) = 0$ and membrane stress resultants $N^0_{\alpha\beta}(\mathbf{x})$ satisfying the in-plane equilibrium equations given in Eq. (S55). Towards this end, we introduce the perturbed quantities about the base state

$$u_3(\mathbf{x}) = u_3^0(\mathbf{x}) + \tilde{u}_3(\mathbf{x}) = \tilde{u}_3(\mathbf{x}), \tag{S66}$$

$$M_{\alpha\beta}(\mathbf{x}) = M^0_{\alpha\beta}(\mathbf{x}) + \tilde{M}_{\alpha\beta}(\mathbf{x}) = \tilde{M}_{\alpha\beta}(\mathbf{x}), \tag{S67}$$

$$N_{\alpha\beta}(\mathbf{x}) = N^0_{\alpha\beta}(\mathbf{x}, \kappa) + \tilde{N}_{\alpha\beta}(\mathbf{x}). \tag{S68}$$

Substitution of Eqs. (S66)–(S68) into Eq. (S65) yields

$$\frac{\partial^2 \tilde{M}_{\alpha\beta}(\mathbf{x})}{\partial x_\alpha \partial x_\beta} + \frac{\partial}{\partial x_\alpha}\left(N^0_{\alpha\beta}(\mathbf{x}, \kappa)\frac{\partial \tilde{u}_3(\mathbf{x})}{\partial x_\beta}\right) + \frac{\partial}{\partial x_\alpha}\left(\tilde{N}_{\alpha\beta}(\mathbf{x})\frac{\partial \tilde{u}_3(\mathbf{x})}{\partial x_\beta}\right) = 0, \tag{S69}$$

which, since the last term is of second order as compared to the first two [10, 11], can be reduced to

$$\frac{\partial^2 \tilde{M}_{\alpha\beta}(\mathbf{x})}{\partial x_\alpha \partial x_\beta} + \frac{\partial}{\partial x_\alpha}\left(N^0_{\alpha\beta}(\mathbf{x}, \kappa)\frac{\partial \tilde{u}_3(\mathbf{x})}{\partial x_\beta}\right) = 0. \tag{S70}$$

Using the constitutive relation given in Eq. (S60), we obtain

$$\frac{\partial}{\partial x_\alpha}\frac{\partial \tilde{M}_{\alpha\beta}(\mathbf{x})}{\partial x_\beta} = -D\left[(1-\nu)\frac{\partial^4 \tilde{u}_3(\mathbf{x})}{\partial x_\alpha^2 \partial x_\beta^2} + \nu\frac{\partial^4 \tilde{u}_3(\mathbf{x})}{\partial x_\alpha^2 \partial x_\beta^2}\right] = -D\frac{\partial^4 \tilde{u}_3(\mathbf{x})}{\partial x_\alpha^2 \partial x_\beta^2} = -D\nabla^4 \tilde{u}_3(\mathbf{x}), \tag{S71}$$

where ∇^4 denotes the biharmonic operator with respect to $\mathbf{x}$. Substituting Eq. (S71) into Eq. (S70) and using Eq.(S63) yield the buckling equilibrium equation in terms of the out-of-plane perturbation $\tilde{u}_3(\mathbf{x})$,

$$D\nabla^4 \tilde{u}_3(\mathbf{x}) - \kappa\frac{\partial}{\partial x_\alpha}\left(N^0_{\alpha\beta}(\mathbf{x})\,\frac{\partial \tilde{u}_3}{\partial x_\beta}(\mathbf{x})\right) = 0. \tag{S72}$$

This equation is solved to determine the critical loading factor κ_{cr}. Note that for an initially flat plate with the membrane resultants as a function of in-plane stresses given in Eq.(S56), Eq. (S72) reduces to

$$D\nabla^4 \tilde{u}_3(\mathbf{x}) - \kappa\frac{\partial}{\partial x_\alpha}\left(t\,\sigma^0_{\alpha\beta}(\mathbf{x})\,\frac{\partial \tilde{u}_3}{\partial x_\beta}(\mathbf{x})\right) = 0. \tag{S73}$$

Next, in subsections IV A and IV B below we specialize Eq. (S72) for a plate with constant height and a plate with periodically modulated height, respectively.

A. Rectangular plate

We begin by considering a rectangular strip, following [12]. Specifically, the reference configuration occupies the domain

$$\Omega = \left\{ 0 \le x_1 \le L, \quad 0 \le x_2 \le H_0, \quad -\frac{t}{2} \le x_3 \le \frac{t}{2} \right\}, \tag{S74}$$

where L and H_0 denote the length, height, and thickness of the plate, respectively. The plate is subjected to an in-plane compressive displacement applied along its bottom edge (Fig. S6).

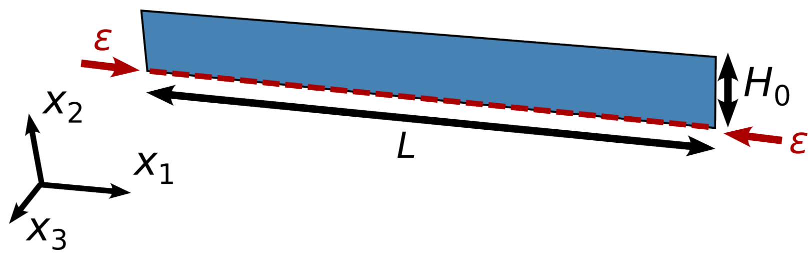

Fig. S6. **A schematic of the rectangular plate.** We consider a thin rectangular plate of length L, height H_0, and thickness (not shown) t in the x_1, x_2, and x_3 directions respectively. We highlight our imposed boundary condition—uniform strain ε along the bottom edge.

Prior to the onset of buckling, the displacement field in the plate is given by [12]

$$u_1^0 = -\kappa x_1, \qquad u_2^0 = 0, \tag{S75}$$

where κ is the loading parameter. Substituting Eq. (S75) into the strain–displacement relations (S50) and the constitutive law (S54) yields the pre-buckling strain field

$$\varepsilon_{11}^0(\mathbf{x}) = -\kappa, \qquad \varepsilon_{22}^0(\mathbf{x}) = 0, \qquad \varepsilon_{12}^0(\mathbf{x}) = 0, \tag{S76}$$

and the corresponding stress field

$$\sigma_{11}^0(\mathbf{x}) = -\frac{\kappa E}{1-\nu^2}, \qquad \sigma_{22}^0(\mathbf{x}) = -\frac{\kappa E \nu}{1-\nu^2}, \qquad \sigma_{12}^0(\mathbf{x}) = 0. \tag{S77}$$

The stress field in Eq. (S77) is then used to compute the resultant membrane stresses $N_{\alpha\beta}^0(\mathbf{x})$ via Eq. (S56), yielding

$$N_{11}^0(\mathbf{x}) = -\frac{\kappa h E}{1-\nu^2}, \qquad N_{22}^0(\mathbf{x}) = -\frac{\kappa h E \nu}{1-\nu^2}, \qquad N_{12}^0(\mathbf{x}) = 0. \tag{S78}$$

These membrane stresses satisfy the in-plane equilibrium equation given by Eq. (S55). Finally, substituting Eq. (S78) into Eq. (S72), the buckling equation becomes

$$D\nabla^4 \tilde{u}_3(\mathbf{x}) + \frac{\kappa t E}{1-\nu^2} \left(\frac{\partial^2 \tilde{u}_3(\mathbf{x})}{\partial x_1^2} + \nu \, \frac{\partial^2 \tilde{u}_3(\mathbf{x})}{\partial x_2^2} \right) = 0, \tag{S79}$$

which is a homogeneous linear partial differential equation in $\tilde{u}_3(\mathbf{x})$ with constant coefficients. This equation defines an eigenvalue problem that is solved to determine the minimum value of κ corresponding to the critical buckling strain, for which nontrivial out-of-plane displacement fields $\tilde{u}_3(\mathbf{x})$ (buckling modes) exist. For a simple rectangular geometry, this problem can be solved analytically by enforcing the boundary conditions and invoking asymptotic assumptions in the $\mathbf{e}_2$ direction to neglect the second term in the parentheses of Eq. (S79). Under these assumptions, an analytical ansatz for the nontrivial solution $\tilde{u}_3(\mathbf{x})$ may be employed [12]. Alternatively, the problem can be solved numerically using the finite element method, for example through a buckling analysis step in ABAQUS.

B. Elastic plate with modulated height

Analogous to a beam resting on a Winkler foundation with constant stiffness, Eq. (S79), which governs the buckling behavior of a rectangular plate, has constant coefficients; however, it is a partial differential equation rather than an ordinary differential equation. In contrast, an elastic beam on a Winkler foundation with periodically modulated stiffness is governed by linear differential equations with periodically varying coefficients. As shown in Fig. S5 and Fig. 1 of the main text, this periodic modulation gives rise to wavenumber lock-in tongues. Motivated by these results, we next modify the plate to identify a physical platform capable of reproducing the same phenomenon. Although such an effect could, in principle, be achieved by introducing a spatially varying Youngs modulus $E(x_1)$, this approach is difficult to realize in practice. Instead, we exploit geometric modulation to induce a periodic variation in the compressive pre-buckling membrane stresses $N^0_{\alpha\beta}(\mathbf{x})$. Specifically, we prescribe a spatially varying plate height according to

$$H(x_1) = H_0 + H_1 \cos\left(\frac{2\pi}{\lambda_{\text{mod}}} x_1\right). \tag{S80}$$

This choice defines a material domain Ω' given by

$$\Omega' = \left\{0 \leq x_1 \leq L,\ 0 \leq x_2 \leq H(x_1),\ -\frac{t}{2} \leq x_3 \leq \frac{t}{2}\right\}. \tag{S81}$$

We see a schematic of our unit cell in Fig. S7a and an example domain in Fig. S7b.

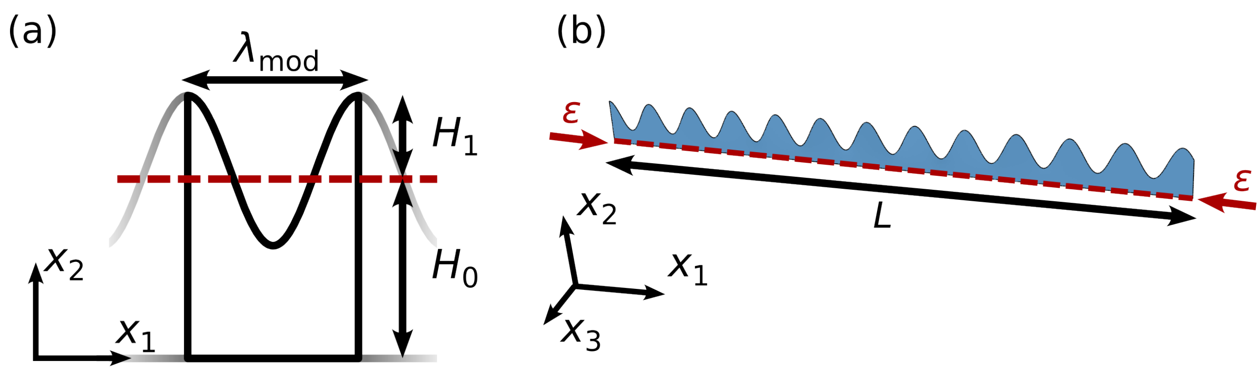

Fig. S7. **A schematic of the elastic plate with modulated height.** (a) Unit cell in the x_1-x_2 plane. (b) An example domain; we highlight the total length of the sample, L. While the thickness of our thin plate, t, is not shown, note that it is the dimension in the x_3 direction. We also highlight our imposed boundary condition—uniform strain ε along the bottom edge.

To handle a domain with spatially varying height, we map Ω' onto an effective domain with constant height via an appropriate coordinate transformation [13]

$$\mathbf{x} = \Phi(\mathbf{y}) = \begin{bmatrix} Ly_1 \\ H(Ly_1)\, y_2 \\ y_3 \end{bmatrix}. \tag{S82}$$

Under this transformation (which we note is a smooth bijection), the domain becomes fixed in the new coordinate system

$$\Omega' = \left\{0 \leq y_1 \leq 1,\ 0 \leq y_2 \leq 1,\ -\frac{t}{2} \leq y_3 \leq \frac{t}{2}\right\}. \tag{S83}$$

Since $H(y_1)$ is λ_{mod}/L-periodic, the transformation inherits this periodicity, satisfying

$$\Phi\left(y_1+\frac{\lambda_{\mathrm{mod}}}{L},\, y_2,\, y_3\right)=\Phi(y_1,y_2,y_3)+\left(\frac{\lambda_{\mathrm{mod}}}{L},\, 0,\, 0\right). \tag{S84}$$

Furthermore, because Φ leaves the x_3 coordinate unchanged and the in-plane coordinates (x_1,x_2) are independent of x_3, the mapping may be written as

$$(x_1,x_2,x_3)=\Phi(y_1,y_2,y_3),=\varphi(y_1,y_2)\times \mathrm{id}, \tag{S85}$$

where φ denotes the two-dimensional in-plane mapping and id is the identity mapping in the thickness direction.

Going forward, we will only consider the subdomains of $\Omega'(\mathbf{x})$ and $\Omega'(\mathbf{y})$ at the mid-plane $x_3=y_3=0$ in the (x_1,x_2) or (y_1,y_2) planes respectively, where φ maps between them (only the two-dimensional coordinate system $\mathbf{x}=x_\alpha\mathbf{e}_\alpha$ is needed in Kirchhoff-Love plate theory). Next, we gain insight into the structure of the pre-buckling membrane stress resultants $N^0_{\alpha\beta}(\mathbf{x})$. To this end, we compute the linearized strain tensor using the strain–displacement relation given in Eq. (S50). Because the in-plane displacement is defined as a function of $\mathbf{y}$

$$\underbrace{u^0_\alpha(\varphi(\mathbf{y}))}_{u^0_\alpha(\mathbf{y})}=u^0_\alpha(\mathbf{x}), \tag{S86}$$

we apply the chain rule to obtain

$$\frac{\partial u^0_\alpha(\varphi(\mathbf{y}))}{\partial y_\beta}=\frac{\partial u^0_\alpha}{\partial x_m}(\mathbf{x})\,\frac{\partial \varphi_m}{\partial y_\beta}. \tag{S87}$$

Equivalently,

$$\frac{\partial u^0_\alpha}{\partial y_\beta}(\mathbf{y})=\frac{\partial u^0_\alpha}{\partial x_m}(\mathbf{x})\,J_{m\beta}, \tag{S88}$$

where we have introduced the Jacobian matrix

$$J_{m\beta}=\frac{\partial \varphi_m}{\partial y_\beta}. \tag{S89}$$

For the mapping $\mathbf{x}=\varphi(\mathbf{y})$, the Jacobian reads

$$J_{m\beta}=\begin{pmatrix} L & 0\\ L y_2\,\dfrac{dH}{d(Ly_1)} & H(Ly_1)\end{pmatrix} \tag{S90}$$

and is $(\lambda_{\mathrm{mod}}/L)$-periodic. Inverting Eq. (S88), the displacement gradients in the physical coordinates can be expressed as

$$\frac{\partial u^0_\alpha}{\partial x_\beta}(\mathbf{x})=\frac{\partial u^0_\alpha}{\partial y_m}(\mathbf{y})\,K_{m\beta}. \tag{S91}$$

with

$$\mathbf{K}=\mathbf{J}^{-1}=\frac{1}{L\,H(Ly_1)}\begin{pmatrix} H(Ly_1) & 0\\ -\frac{\partial H(Ly_1)}{\partial(Ly_1)}Ly_2 & L\end{pmatrix}. \tag{S92}$$

Finally, substitution of Eq. (S91) into Eq. (S50) yields

$$\varepsilon^0_{\alpha\beta}(\mathbf{x}) = \frac{1}{2}\left(\frac{\partial u^0_\alpha}{\partial y_m}(\mathbf{y})K_{m\beta} + \frac{\partial u^0_\beta}{\partial y_m}(\mathbf{y})K_{m\alpha}\right). \tag{S93}$$

When the plate is subjected to an in-plane compressive displacement along its bottom edge, the pre-buckling displacement field is given by Eq. (S75). Consequently, the partial derivatives of $u^0_\alpha(\mathbf{y})$ with respect to $\mathbf{y}$ are constant. Because these derivatives are constant while the Jacobian matrix $\mathbf{K}$ of Eq. (S92) is $(\lambda_{\mathrm{mod}}/L)$-periodic, the quantities $\partial u^0_\alpha/\partial x_\beta$ inherit the periodicity of the Jacobian. It therefore follows that

$$\frac{\partial u^0_\alpha}{\partial x_\beta}(x_1, x_2) = \frac{\partial u^0_\alpha}{\partial x_\beta}(x_1 + \lambda_{\mathrm{mod}}, x_2) \qquad \text{and} \qquad \varepsilon^0_{\alpha\beta}(x_1, x_2) = \varepsilon^0_{\alpha\beta}(x_1 + \lambda_{\mathrm{mod}}, x_2). \tag{S94}$$

Importantly, we can see from Eq. (S54) and (S56) that a λ_{mod}-periodic pre-buckling strain tensor $\varepsilon^0_{\alpha\beta}(\mathbf{x})$ necessarily implies λ_{mod}-periodic stresses $\sigma^0_{\alpha\beta}(\mathbf{x})$ and membrane stress resultants, $N^0_{\alpha\beta}(\mathbf{x})$,

$$\sigma^0_{\alpha\beta}(x_1, x_2) = \sigma^0_{\alpha\beta}(x_1 + \lambda_{\mathrm{mod}}, x_2), \tag{S95}$$

$$N^0_{\alpha\beta}(\mathbf{x}) = N^0_{\alpha\beta}(x_1, x_2) = N^0_{\alpha\beta}(x_1 + \lambda_{\mathrm{mod}}, x_2) \tag{S96}$$

$$\frac{\partial N^0_{\alpha\beta}(x_1, x_2)}{\partial x_\alpha} = \frac{\partial N^0_{\alpha\beta}(x_1 + \lambda_{\mathrm{mod}}, x_2)}{\partial x_\alpha} \tag{S97}$$

The periodicity of the pre-buckling stress in the plate with modulated height is further confirmed by finite-size finite element simulations performed in Abaqus. As shown in Fig. S8a, we monitor the stress along a horizontal line. In Fig. S8b, we plot the average stress σ^0_{11} of each element along this line as a function of the element centroid, and observe that the stress distribution is nearly periodic, with a period very close to λ_{mod}.

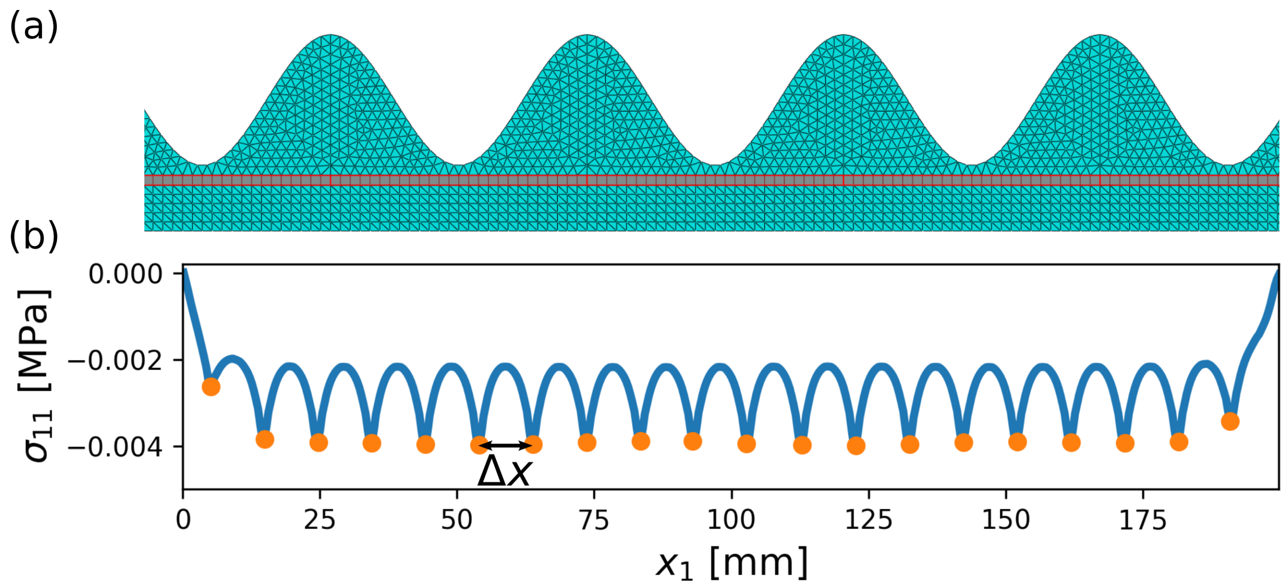

Fig. S8. **Periodic stress in wavy strip** (a) We mesh the strip with a line of quadrilateral elements. (b) For $\lambda_{\mathrm{mod}} = 9.8$ mm and $H_1/H_0 = 0.5$, we plot σ_x along this line of elements at $\varepsilon = -0.016$. We see that our stress σ_{11} is periodic as expected. We calculate that $\Delta x = 9.78 \pm 0.15$ mm

Finally, Eqs. (S95)–(S97) imply that the governing buckling equation (S72) or (S73) for an elastic plate with periodically modulated height has λ_{mod}-periodic coefficients and is therefore expected to exhibit wavenumber lock-in tongues.

V. FINITE ELEMENT SIMULATIONS

We performed Finite Element (FE) simulations of the modulated thin strip using the commercial software packages Abaqus 2019/Standard and 2021/Standard. Two types of simulations were carried out: (1) finite-size simulations, using either a buckling step or modeling the post-buckling response, and (2) Bloch wave simulations conducted on a single periodic unit cell.

All models were meshed with shell elements, S3 or S4R, with an out-of-plane Poisson's ratio specified as $\nu = 0.49$. This shell-specific Poisson's ratio controls the change in thickness due to in-plane membrane strain. For the material, we use an incompressible Neo-Hookean material model.

A. Finite size simulations

We simulate finite size samples over a variety of lengths, ranging from $L = 200$ mm (matching the experimental samples) to $L = 1200$ mm. Since the period of modulation, λ_{mod} will not always divide evenly into the total length, some simulations have a non-integer number of periods; this did not affect our results. To impose uniform compression along the bottom edge, we set our boundary condition by constraining the x-displacement for every point along the bottom edge. We conducted two types of finite size simulations: (1) linear buckling analyses and (2) post-buckling analyses, using one of the eigenmodes from the linear buckling analysis as a geometric imperfection.

A.1. Linear buckling analyses

From each linear buckling analysis, we extract the displacement in the x_3 direction as a function of original x_1 coordinate of the top edge of our strip (Fig. S9a). We seek to extract spectral information about the displacement using the discrete Fourier transform (DFT). In the modulated case, our mesh is not guaranteed to be uniformly spaced in x_1, so we first linearly interpolate the u_3 with 100 points per period. We then take the DFT over our function $u_3(x_1)$ and find the wavenumber $\tilde{\nu}$ associated with the largest peak magnitude (Fig. S9b). To ensure the binning is not an issue, we zero-pad our data to have a total length of $n_{\text{fft}} = 2^{14}$.

a. Unmodulated case: $H_1 = 0$. We first validate our simulations in the unmodulated case, where analytical work has shown that for thin strips of height H_0 subject to compressive loads along their bottom edge, the wavelength of the top edge should be [12]

$$\lambda_{\text{rec}} = 3.256 H_0. \tag{S98}$$

We compare this analytical result to our simulations by calculating $\lambda_{cr} = 1/\tilde{\nu}$ (Fig. S9b). This comparison can be seen in Fig. S9c, and we see good results. We also observe that as our finite length L increases, we see better matching with the theory, since the number of periods L/λ_{mod} increases. This motivates our usage of periodic unit cell simulations, discussed below, as we would like to calculate the critical wavenumbers for our system without having to use a very large L.

b. Modulated case: $H_1 > 0$. In the modulated case, we still look for the location of the wavenumber associated with the largest peak. This gives us a single wavenumber; however, we can calculate all the valid wavenumbers in the reciprocal space via

$$\tilde{\nu}^* = \frac{n}{\lambda_{\text{mod}}} \pm \tilde{\nu} \;\text{ for }\; n \in \mathbb{Z}. \tag{S99}$$

This equation comes from the Bloch wave conditions and is equivalent to our Floquet exponents s_i being separated by $h\bar{\Omega}$ in our earlier analysis. While finite size simulations are an approximation of the infinite solution, as long as our sample is long enough, we can assume this equation holds. In the same way as the Winkler foundation, we see periodic solutions when our normalized wavenumber, $\tilde{\nu}\lambda_{\text{mod}}$, has a value of $0.5 + k$ or $0 + k$ for $k \in \mathbb{Z}$. Otherwise, our solutions are quasi-periodic. We plot the locations of our peaks (black) and our extended spectra (gray) as a function of λ_{mod} at $H_1/H_0 = 0.5$ in Fig. S10c.

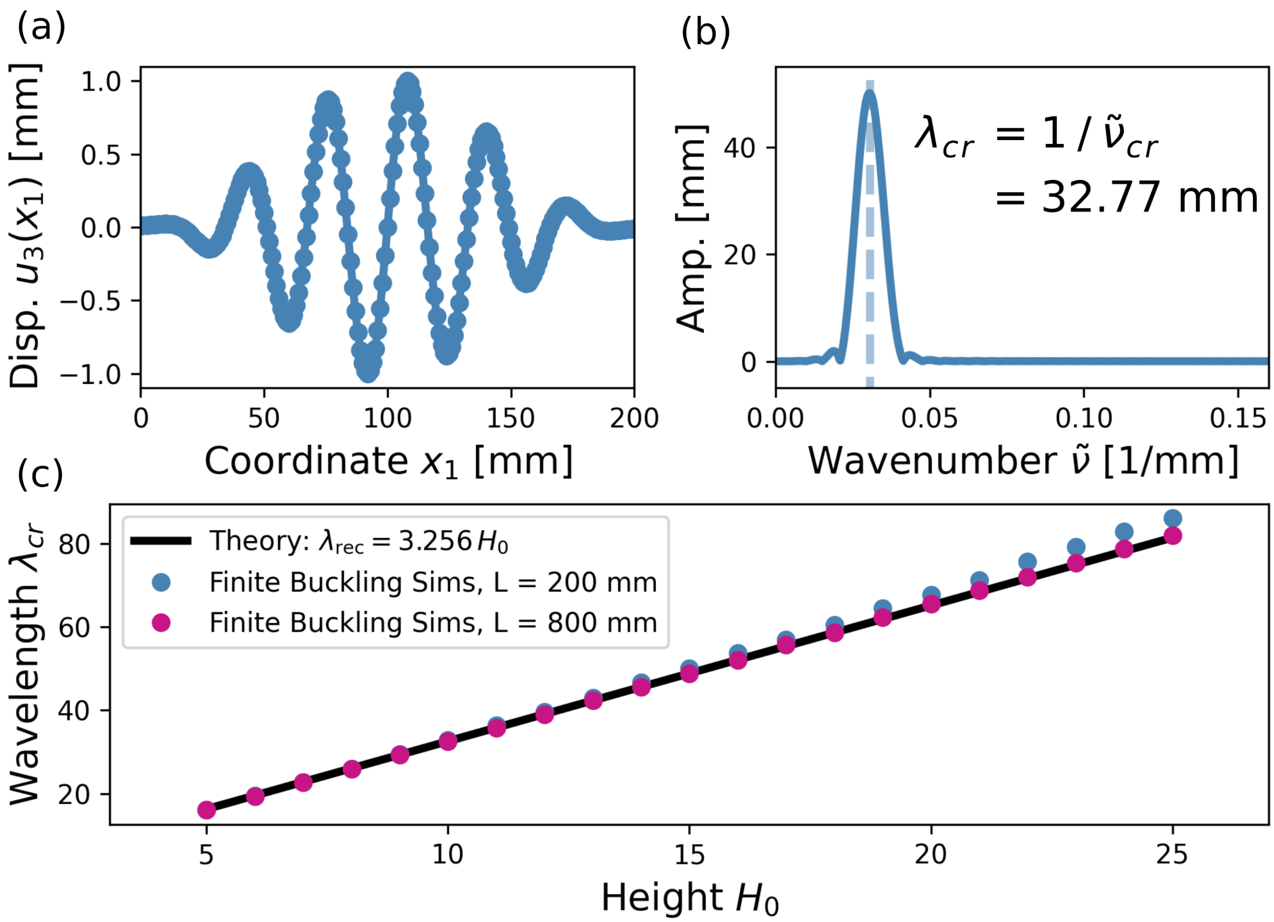

Fig. S9. **Validation of unmodulated theory for finite length simulations** (a) Deformation of the first linear buckling mode for $H_0 = 10$ mm (b) DFT of that mode; we locate the wavenumber associated with the peak and calculate the wavelength of the mode. (c) Wavelength as a function of H_0; we see that our FE simulations match theory.

A.2. Post-buckling analyses

Besides linear buckling analyses, we also perform static analyses into the postbuckling regime. The main purpose of these is as a closer comparison to our experiments, where we measure in the postbuckled state and where the total length of our sample is a limiting factor. All models used in our post-buckling simulations have $L = 200$ mm, to match with experimental samples and were compressed to 10 mm (except the samples for $\lambda_{\mathrm{mod}} = 8.2$ and 12.2 mm, which were compressed to 13 and 12 mm, respectively) to match experiments. We additionally use these analyses to check that performing our analysis in the post-buckling regime does not change the location of the peak wavenumber, $\tilde{\nu}_{cr}$.

To ensure that the structure buckles upon compression, we introduce an imperfection into the mesh in the form of the most critical eigenmode. The mesh is perturbed by the first eigenmode, $\mathbf{v}_1$, scaled by the scale factor ϵ

$$\mathbf{X}^{\mathrm{postbuckling}} = \mathbf{X}^{\mathrm{original}} + \epsilon \mathbf{v}_1, \tag{S100}$$

where $\mathbf{X}^{\mathrm{postbuckling}}$ and $\mathbf{X}^{\mathrm{original}}$ are the modified and original coordinates of our model, respectively and ϵ is some scalar parameter that controls how much we edit our initial mesh; in this work we use $\epsilon = 0.05t$, where t is the thickness of our strip in the x_3 direction.

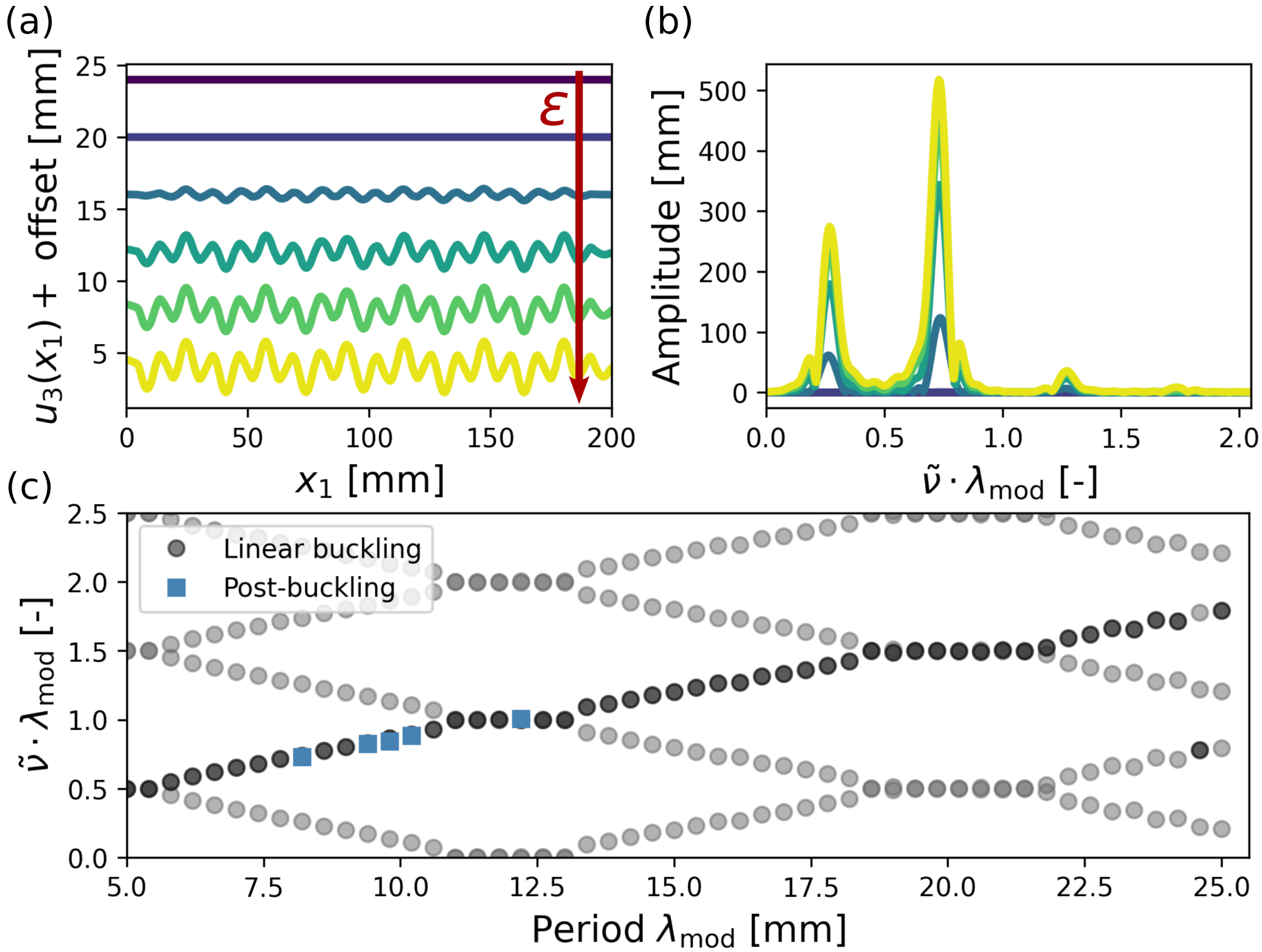

Fig. S10. **Validation of postbuckling simulations** (a) Deformation of the top edge $u_3(x_1)$ for a simulation $\lambda_{\mathrm{mod}} = 8.2$ mm, $H_1/H_0 = 0.5$ with increasing strain. (b) We see that the locations of the peaks do not significantly move in the post-buckling regime. (c) Our post-buckling simulations ($L = 200$ mm) have the same fundamental peak locations as linear buckling simulations ($L = 1200$ mm).

In Fig. S10a, we plot several snapshots of the top edge displacement, $u_3(x_1)$, at increasing strains for a strip with $H_1/H_0 = 0.5$ and $\lambda_{\mathrm{mod}} = 8.2$ mm. We calculate the DFTs of each of those curves and plot those in Fig. S10b. We see that once peaks appear (after buckling onset), their locations do not substantially change with increasing deformation. We then plot the location of the highest peak from the final frame of our postbuckling simulations against the extended spectra from linear buckling simulations (Fig. S10c); we see that the postbuckling simulations have the same peak locations as the linear buckling simulations.

B. Bloch wave simulations

We also investigate the behavior of infinite periodic strips using simulations of a single unit cell [14]; in the modulated case, this unit cell has length λ_{mod}, while in the unmodulated case, its length is arbitrary; we denote the length of our unit cell as L^*. To study the buckling of our structure, we first compress our unit cell to some strain ϵ, then investigate the frequency response of small-amplitude waves of linear wavenumber $\tilde{\nu}$. We know the response of a wave through a system looks like [15]

$$u(x,t) = u_0(x)\, e^{i\omega t}, \tag{S101}$$

so if ω is real, then $u(x,t)$ describes a stable perturbation. However, if ω is instead imaginary, then $u(x,t)$ grows unstably. We therefore look for the onset of this instability, when ω transitions from real to imaginary—where $\omega^2 = 0$. The wavenumber of the buckled state and the infinite periodic solution can then be extracted from the deformed state. To test the frequency response of a wavenumber $\tilde{\nu}$, we use Bloch wave boundary conditions along the vertical edges of our unit cell. These boundary conditions relate the deformation of the right side $\mathbf{u}^{\mathrm{right}}$ to the left $\mathbf{u}^{\mathrm{left}}$ as

$$\mathbf{u}^{\mathrm{right}} = \mathbf{u}^{\mathrm{left}}\, e^{i2\pi\tilde{\nu}L^*}, \tag{S102}$$

where L^* is the undeformed length of our sample and is equal to λ_{mod} for the modulated simulations. We pick $\tilde{\nu}$ in the first Brillouin zone, i.e. $\tilde{\nu} \in [0, 1/L^*)$. Practically, we know neither the buckling wavenumber $\tilde{\nu}$ nor the strain ϵ at which the structure buckles, so to find both we sweep over many values of ϵ and look for the lowest strain at which there is a 0-frequency response.

We simulate this process in ABAQUS Standard/2021, using a *STATIC step for the deformation of the unit cell up to ϵ and a *FREQUENCY step for the eigenfrequency analysis. At each Frequency step, the boundary condition from Eq. (S102) is changed to test a new value for $\tilde{\nu}$. In this work, we used 50 Frequency steps for each geometry, which is equivalent to testing 50 values of $\tilde{\nu} \in [0, 1/L^*)$. Additionally, because Abaqus cannot handle complex values as those required to prescibe the boundary conditions defined by Eq. (S102), we split our unit cell into two identical unit cells with the same mesh. One handles the real component of the deformation, while the other handles the imaginary component of the deformation [16].

a. Unmodulated case: $H_1 = 0$. As with the finite sized simulations, we first seek to validate our Bloch wave simulations by checking that the theory from Eq. (S98) holds. While for the unmodulated case, we can choose L^* arbitrarily, we pick $L^* = H_0$, so that the expected fundamental wavenumber, $\tilde{\nu}_{cr} = 1/(3.256\, H_0)$, lies within the lower half of the first Brillouin zone, i.e. $\tilde{\nu}L^* \in [0, 0.5]$. We see an example of this process for $H_0 = L^* = 15$ mm in Fig. S11a. Because we plot the critical wavelength, $1/\tilde{\nu}_{cr}$, we are especially sensitive to small errors in the critical wavenumber, $\tilde{\nu}_{cr}$. Therefore, instead of simply taking the wavenumber $\tilde{\nu}_{cr}$ with the lowest critical strain, we fit a fourth order spline to the data points around that minimum and find the local minimum of that fit spline (Fig. S11b). We then use that calculated $\tilde{\nu}_{cr}$ to find the critical wavelength for that given geometry; as shown in Fig. S11c, we find good matching with the theory.

b. Modulated case: $H_1 > 0$. We perform the same strain sweep in the modulated case, using the critical strains from finite simulations as initial guesses and only checking strain values around that guess. An example of this process for $\lambda_{\mathrm{mod}} = 11.4$ mm and $H_1/H_0 = 0.25$ can be seen in Fig. S12a. As seen in the main text, we perform this process for many geometries; we see in Fig. S12c that for $H_1/H_0 = 0.25$, the extended spectra of the finite buckling and Bloch wave analysis simulations match well, validating our implementation of the periodic unit cell simulations.

Having identified the critical strain ϵ_{cr}, the buckling mode of the strip can be determined from the critical eigenmode of the two meshes, defined by $\mathbf{u}^{\mathrm{Re}}$ and $\mathbf{u}^{\mathrm{Im}}$ (Fig. S12b), as

$$\mathbf{u}(x_1) = \mathbf{u}^{\mathrm{Re}}(x_1^*) \sin 2\pi L^*\eta + \mathbf{u}^{\mathrm{Im}}(x_1^*) \cos 2\pi L^*\eta, \tag{S103}$$

where $x_1^* = x_1/L^*$ and $\eta = \lfloor x_1/L^* \rfloor$. To calculate the fundamental wavenumber, we can reconstruct the deformation of the top edge, $u_3(x_1)$, to some large length $\ell \gg L^*$ and calculate the peak $\tilde{\nu}$ of the DFT.

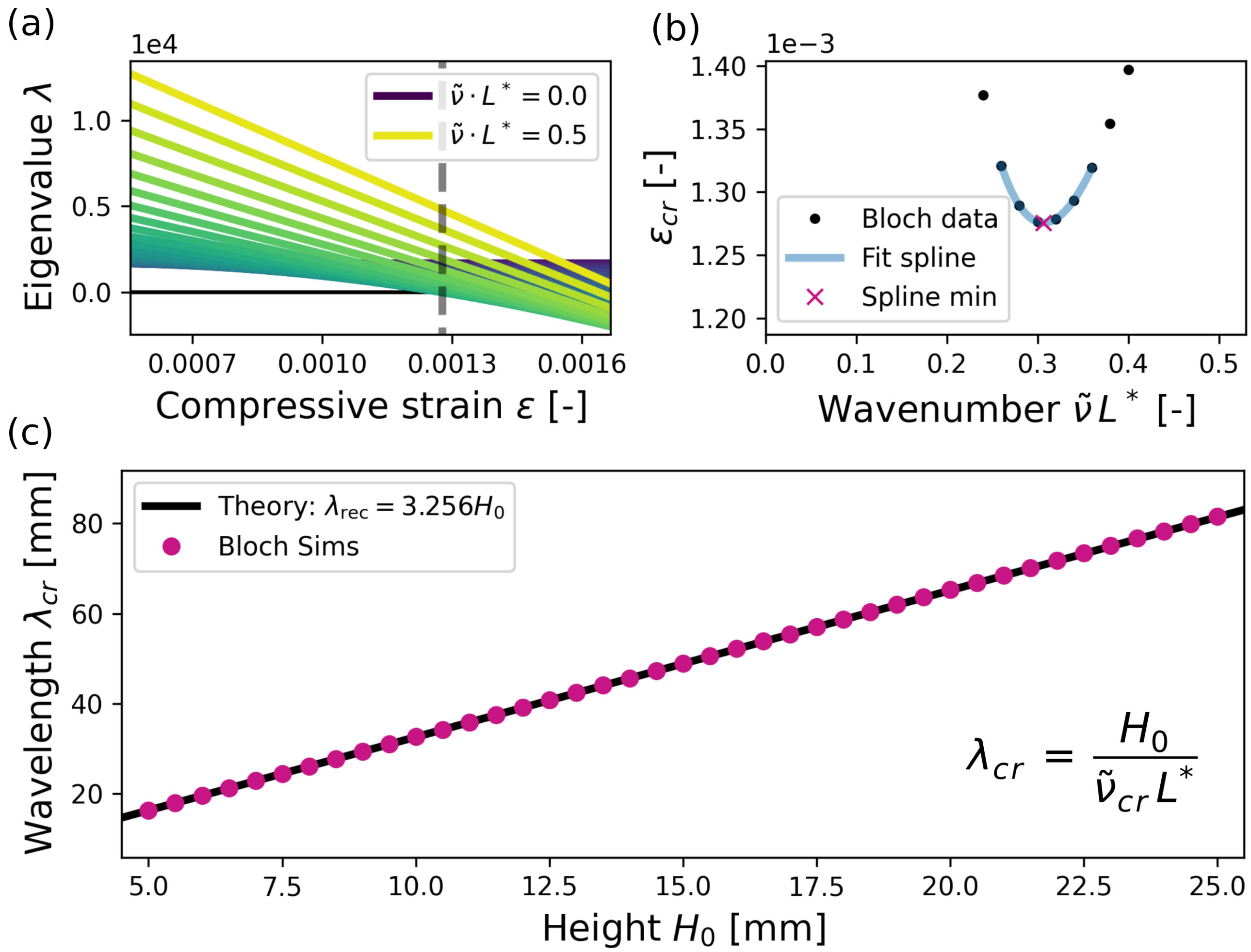

Fig. S11. **Validation of unmodulated theory for Bloch wave simulations** (a) For a given geometry (here, $H_0 = 15$ mm), we sweep over many wavenumbers $\tilde{\nu}$ at different strains ϵ. (b) Each wavenumber $\tilde{\nu}$ yields a 0-frequency response at a different strain, ϵ_{cr}; we fit a spline to determine the minimum of the underlying function. (c) Using the calculated $\tilde{\nu}_{cr}$, we calculate the critical wavelength and compare to the theoretical result.

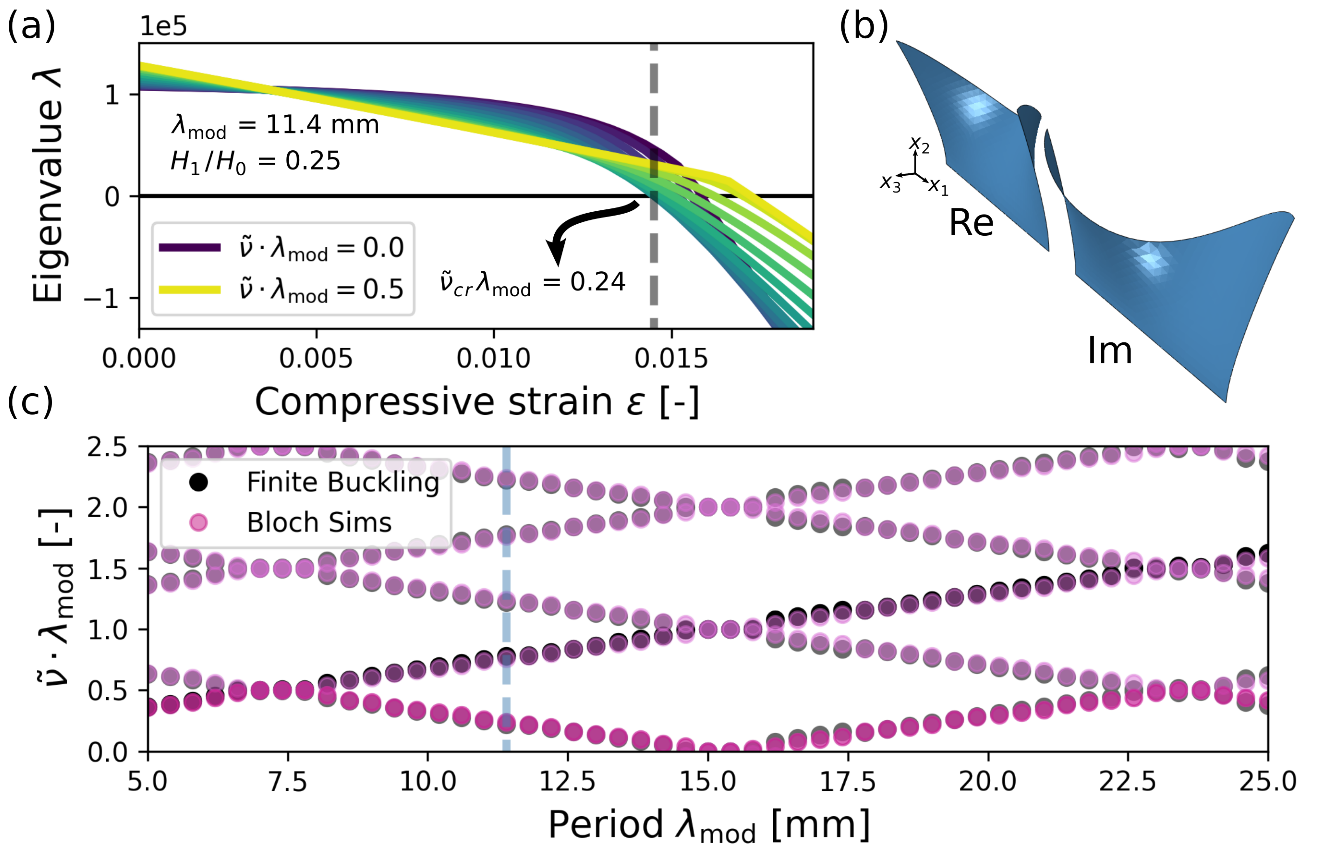

Fig. S12. **Modulated Bloch wave results** (a) We search for both the critical strain ϵ_{cr} and the wavenumber $\tilde{\nu}_{cr}$ for each geometry. (b) The deformation of the complex unit cell at that critical strain; we can use its deformation to reconstruct the infinite solution. (c) Comparison of finite linear buckling simulations with $L = 1200$ mm to Bloch wave simulations for $H_1/H_0 = 0.25$.

VI. FABRICATION

The blocks used in this study are made of nearly incompressible polyvinylsiloxane (PVS) elastomers. We use Elite Double 32 from Zhermack (with green color). The structures are fabricated as a single part using a two-step casting process. In the first step, the thin modulated strip is molded onto a thin supporting block with an out-of-plane thickness of 12.7 mm. In the second step, the block thickness is increased to 40.0 mm to apply the appropriate boundary conditions to the bottom edge of the strip. This two-step approach is necessary because direct molding of the thin modulated layer onto a thick substrate consistently led to cracking in the modulated region during demolding. Importantly, the final block thickness must be sufficiently large to prevent deformation of the block itself under compressive loading, ensuring that buckling occurs only in the modulated strip as intended.

The following step-by-step process is followed:

1. **Mold Preparation for the modulated strip on a thin block:** We laser-cut four acrylic parts with 6.35 mm thickness to form the mold for the modulated strip on a thin block, as illustrated in Fig. S13a. The black part (part #2) has the desired wavy pattern engraved (highlighted in Fig. S14). The depth of the mold can be tailored by adjusting the laser power during manufacturing. To facilitate demolding, all molds are coated with Mann Release Mold 200.

2. **Casting the modulated strip on a thin block:** Parts #1 and #2 are stacked and aligned using four pins (Fig. S13b). The assembly is then filled with uncured PVS elastomer (Fig. S13c).

3. **Closure and Curing:** Parts #3 and #4 (Fig. S13d) are placed on top of the assembly, and pressure clamps are used to ensure uniform thickness (Fig. S13e). The elastomer is cured at room temperature (25 °C) for 30 minutes before demolding. At this point, the modulated strip on a thin block is ready.

4. **Mold Preparation for thickening the block:** A box with two open faces is 3D printed using a BambuLab X1 Carbon printer. Additionally, two top and bottom acrylic plates are laser-cut to enclose the box.

5. **Final casting and curing:** The cured modulated strip on a thin block is placed at the center of the bottom plate (Fig. S13f). The curing box is assembled, and the uncured PVS elastomer mixture is poured inside (Fig. S13g). The assembly is cured at room temperature (25 °C) for 30 minutes.

6. **Finishing Touches:** The edges of the wavy pattern are manually colored black using a Sharpie.

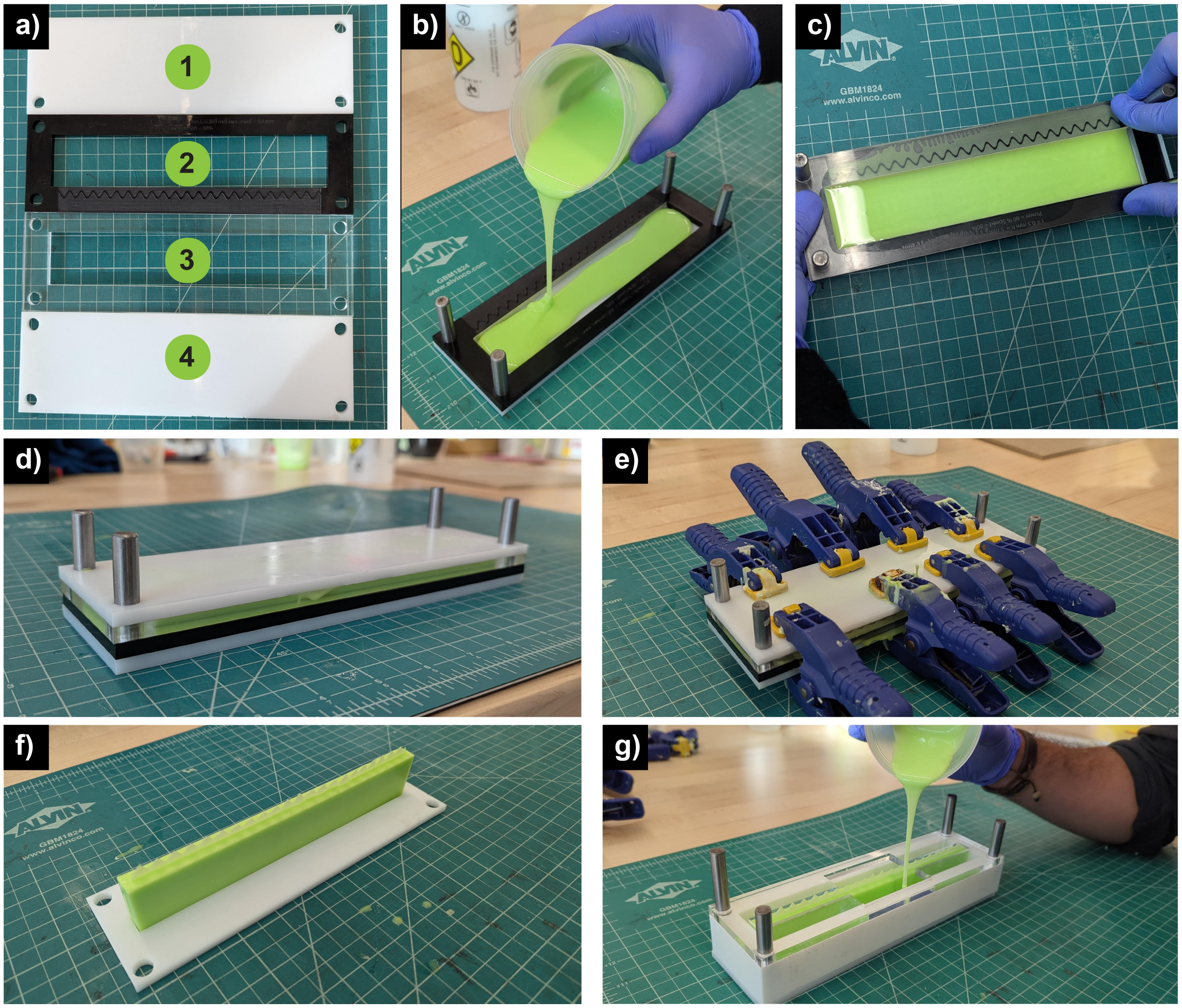

Fig. S13. **Snapshots of the main steps required to fabricate our structures.** (a) We laser cut plates to mold the sample: (1) bottom plate, (2) spacer plate containing laser-etched oscillation (3) spacer plate, (4) top plate. (b) We pour liquid silicone into the cavity formed by stacking the etched plate (2) onto the bottom plate (1). (c) Thin layer containing the wavy pattern is cast by sandwiching plates (2) and (3). (d) Top plate is stacked on top to seal the mold. (e) Clamps are used to squeeze the stacked layers together and get rid of excess material. (f) Central cast containing the oscillating pattern on top is de-molded. (g) We thicken the base by placing the central cast (f) in the middle of a mold and pouring rubber around.

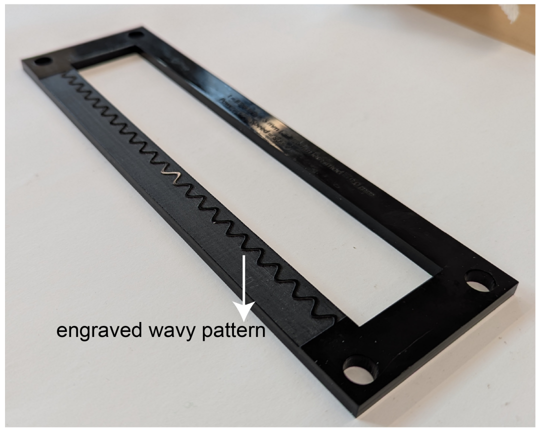

Fig. S14. Laser cut mold with engraved waving pattern on its edge.

VII. TESTING

Our samples are compressed using a universal testing machine (Instron 5969, outfitted with a 2530-series 500-N load cell). To compress the samples uniformly, we place them within the flat circular clamps (Fig. S15). The deformations of the painted edge are captured with a camera and post-processed with the OpenCV library in Python.

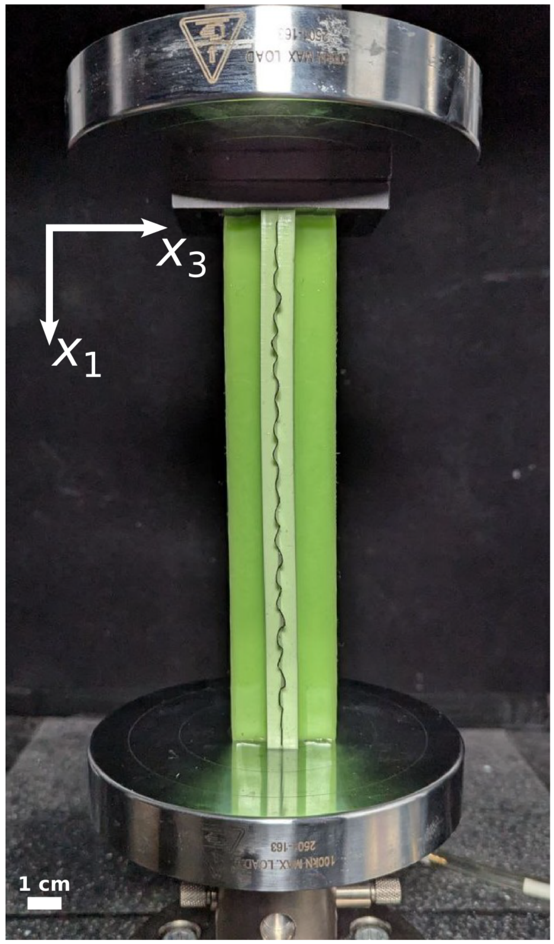

Fig. S15. Example of compression test of a structure with $\lambda_{\mathrm{mod}} = 8.2$ mm.

In order to make the FFTs shown in Fig. 3 of the main text, we need to calculate the top displacement, $u_3(x_1)$ as a function of the original x_1 coordinate. To calculate $u_3(x_1)$, we

1. Post-process the undeformed sample to calculate the location of the top edge in the reference configuration. We define these locations to be $(x_1, x_3(x_1))$.

2. Post-process the deformed edge to calculate the location of the top edge in the current configuration. We define this to be $(x_1^{\mathrm{final}}, x_3(x_1^{\mathrm{final}}))$.

3. Using the known global deformation, u_1, project the deformed coordinates $(x_1^{\mathrm{final}}, x_3^{\mathrm{deformed}}(x_1^{\mathrm{final}}))$ back into the reference frame to calculate $(x_1, x_3^{\mathrm{deformed}}(x_1))$.

4. Calculate $u_3(x_1) = x_3^{\mathrm{deformed}}(x_1) - x_3(x_1)$

5. Calculate the DFT of $u_3(x_1)$ with $n_{\text{fft}} = 2^{14}$

All our experimental results can be seen in Fig. S16. We find strong agreement for $\lambda_{\text{mod}} = 8.2$ mm and 12.2 mm, and moderate agreement for all other samples.

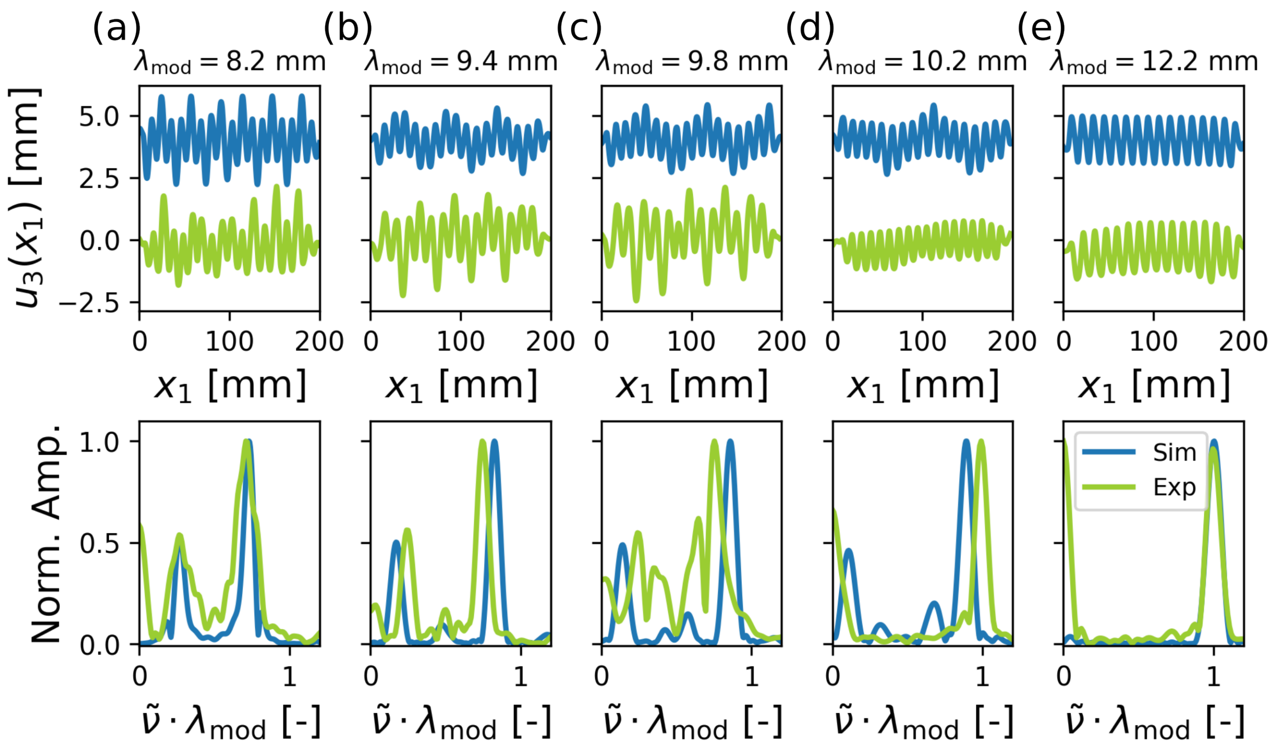

Fig. S16. **Experimental data** All experimental samples (green) compared with post-buckling simulations (blue) for $\lambda_{\text{mod}} = 8.2$, 9.4, 9.8, 10.2, and 12.2 mm. ((a)-(e) respectively)

In order to better understand the disagreement found between FE simulations and experiments for the strip with a wavelength of 9.8 mm, we investigate the sensitivity of our wavy strips to imperfections. Towards this end, we calculate the first 5 linear buckling modes for $\lambda_{\text{mod}} \in [8.2, 20]$ mm while keeping $H_1/H_0 = 0.5$. In Fig. S17a we report the values of those first five buckling eigenvalues λ_i, normalized by the eigenvalue associated with the first mode, λ_1. We see that when our structure is locked-in (periodic buckling mode), the eigenvalues corresponding to each mode are further apart than when the structure is quasi-periodic. Additionally, in Fig. S17b, we plot the normalized wavenumber of each of those first 5 modes; we see that modes which have overlapping eigenvalues have overlapping wavenumbers as well. For example, at $\lambda_{\text{mod}} = 9.8$ mm, the first two critical eigenvalues have a difference of 2.00×10^{-4} and have identical normalized wavenumbers. This separation of eigenvalues suggests that all quasi-periodic geometries are more sensitive than periodic geometries to imperfections. While this does not provide an explanation for why the $\lambda_{\text{mod}} = 8.2$ sample was well behaved while the $\lambda_{\text{mod}} = 9.8$ mm sample was not, it is likely because both are sensitive to small imperfections introduced by casting these thin strips.

[1] A. Lazarus, C. Maurini, and S. Neukirch, in *Extremely Deformable Structures* (Springer, 2015) Chap. 1, pp. 1–53.
[2] F. Brau, P. Damman, H. Diamant, and T. A. Witten, Soft Matter **9**, 8177 (2013).
[3] R. Lagrange and D. Averbuch, International Journal of Mechanical Sciences **63**, 48 (2012).
[4] J. A. Richards, *Analysis of periodically time-varying systems* (Springer Science & Business Media, 2012).

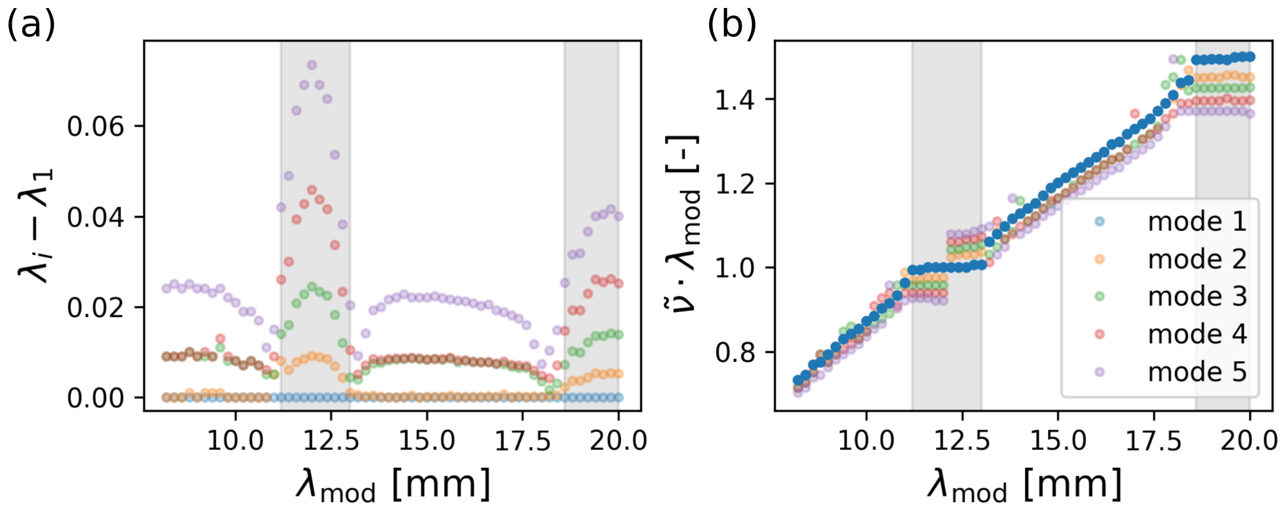

Fig. S17. **First five linear buckling modes for** $H_1/H_0 = 0.5$ (a) Eigenvalues of the first five modes normalized by the eigenvalue of the first mode; we see all 5 modes separate when the structure exhibits a periodic response. (b) Normalized wavenumbers for the first five modes for each value of λ_{mod}. Periodic regions of both plots are highlighted in grey.

[5] R. A. Calico and W. E. Wiesel, Journal of Guidance, Control, and Dynamics **7**, 671 (1984).
[6] G. W. Hill, Acta Mathematica **8**, 3 (1886).
[7] B. Deconinck, F. Kiyak, J. D. Carter, and J. N. Kutz, Mathematics and Computers in Simulation **74**, 370 (2007).
[8] B. Bentvelsen and A. Lazarus, Nonlinear Dynamics **91**, 1349 (2018).
[9] J. Zhou, T. Hagiwara, and M. Araki, Systems & control letters **53**, 141 (2004).
[10] B. Audoly and Y. Pomeau, in *Peyresq lectures on nonlinear phenomena* (World Scientific, 2000) pp. 1–35.
[11] S. P. Timoshenko and S. Woinowsky-Krieger, *Theory of Plates and Shells* (McGraw-Hill, New York, 1959).
[12] T. Mora and A. Boudaoud, The European Physical Journal E **20**, 119 (2006).
[13] P. G. Ciarlet, Journal of elasticity **78**, 1 (2005).
[14] J. Liu and K. Bertoldi, Proc. R. Soc. A **471**, 20150493 (2015).
[15] L. Brillouin, *Wave propagation in periodic structures*, 1st ed. (McGraw-Hill New York, 1946).
[16] M. Åberg and P. Gudmundson, The Journal of the Acoustical Society of America **102**, 2007 (1997).